Research Square

Preprints are preliminary reports that have not undergone peer review.
They should not be considered conclusive, used to inform clinical practice,
or referenced by the media as validated information.

The Role of Quasiperiodicity on the Electronic Structure of Elements

Satish Prajapati

iamsatish.gcect.ac@gmail.com

Government College of Engineering And Ceramic Technology https://orcid.org/0009-0006-3801-1137

Research Article

Keywords: Density of states (DOS), Fermi level, Electronic structure, Pseudogap, Quasicrystals, Quasiperiodic monolayers, Approximants, Density functional theory (DFT), Kernel polynomial method (KPM), Pair distribution function, Fermi surface, Fourier components, Hume-Rothery mechanism, s-d hybridization, Alloy engineering, Orbital engineering, Quantum transport, Berry curvature, Alkali metal monolayers, electronic structure

Posted Date: March 25th, 2026

DOI: https://doi.org/10.21203/rs.3.rs-9203395/v1

License: This work is licensed under a Creative Commons Attribution 4.0 International License.
Read Full License

Additional Declarations: The authors declare no competing interests.

The Role of Quasiperiodicity on the Electronic Structure of Elements

Satish Prajapati[1*] (Corresponding author)
Department of Ceramic Technology, Government College of Engineering and Ceramic Technology,
Kolkata, West Bengal 700010, INDIA
*Corresponding Author: Satish Prajapati (Email: iamsatish.gcect.ac@gmail.com)

Abstract

The discovery of quasicrystals established that long-range atomic order does not require translational periodicity. Yet whether quasiperiodic order alone determines electronic structure—specifically the pseudogap at the Fermi level—remains unresolved. Here we present a definitive computational test using alkali metal (Na, K) monolayers on icosahedral Al-Pd-Mn, a system where quasiperiodic order is isolated from chemical complexity. Contrary to the prevailing hypothesis, we find no pseudogap in these perfectly ordered quasiperiodic monolayers. The density of states is indistinguishable from free-electron behavior with $N(E_F) = 0.32 \pm 0.03$ (Na) and 0.28 ± 0.03 (K) states/eV/atom. The quasiperiodic potential strength is an order of magnitude too weak (| $V(\mathbf{G}_{\parallel})$ |≈ 0.05 eV), and the Hume-Rothery condition $2k_F =$| $\mathbf{G}_{\parallel}$ | fails by 8% (Na) and 12% (K). Orbital decomposition reveals negligible s-d hybridization with charge transfer $<0.05e$ per atom. These results establish that quasiperiodicity alone is insufficient to induce a pseudogap; strong orbital hybridization and precise Fermi surface resonance are required. We present a unified phase diagram that collapses all calculated data onto a single scaling function, enabling quantitative predictions for strain engineering (8% tensile on Na) and alloying (7% Pb in Na). This work resolves a fundamental question in quasicrystal physics and provides design principles for aperiodic materials.

1. Introduction

The 1984 discovery of a metallic phase with ten-fold diffraction symmetry [1] shattered the crystallographic paradigm that long-range order necessitates translational periodicity. Quasicrystals—structures that are ordered but not periodic—exhibit a characteristic electronic signature: a pseudogap at the Fermi level E_F [2–5], linked to high resistivity and anomalous transport [6–8].

A central question has persisted for four decades: is the pseudogap a universal consequence of quasiperiodic order, or does it require specific chemical and electronic conditions? Testing this

has proven difficult. Bulk quasicrystals contain multiple elements with complex d-p hybridization [9,10]. Surface studies on p-block elements (Pb, Sn, Bi) show pseudogaps correlated with hybridization strength [11,12], leaving s-electron systems—which should exhibit the weakest hybridization—unexplored.

We address this gap by studying alkali metal (Na, K) monolayers on icosahedral Al-Pd-Mn. The substrate provides a well-characterized quasiperiodic template [13]; the overlayer consists of simple s-electron metals [14]; monolayer thickness ensures electronic structure is determined primarily by the quasiperiodic potential [15]; and the absence of strong d-orbital contributions eliminates confounding hybridization effects.

Using density functional theory (DFT) on periodic approximants and the kernel polynomial method (KPM) [16], we demonstrate that quasiperiodic Na and K monolayers exhibit no pseudogap at E_F. The density of states (DOS) is nearly free-electron-like, the quasiperiodic potential is an order of magnitude weaker than in the substrate, and the Hume-Rothery condition fails. These findings establish that quasiperiodicity alone is insufficient to induce a pseudogap; strong orbital hybridization and precise Fermi surface resonance are required.

---

2. Results

2.1 Structural Ordering

Na and K form well-ordered quasiperiodic monolayers on i-Al-Pd-Mn(111). Na atoms occupy hollow sites of pseudo-Mackay clusters, forming a quasiperiodic array with Na-Na distances following the Fibonacci sequence:

$$d_n = d_{\min}\tau^n, d_{\min} = 4.8\ \text{Å}, \tau = 1.618 \qquad (1)$$

Peaks in the pair distribution function $g(r)$ appear at 4.8, 7.8, and 12.6 Å. K exhibits analogous ordering with $d_{\min} = 5.2$ Å. Binding energy distributions reveal two distinct local environments: cluster centers (-1.82 eV for Na, -1.65 eV for K) and inter-cluster sites (-1.68 eV for Na, -1.52 eV for K). Simulated LEED patterns exhibit sharp ten-fold spots, confirming long-range quasiperiodic order. (Full characterization in Figs. 1–3)

2.2 The Pseudogap is Absent

The clean i-Al-Pd-Mn substrate exhibits a deep pseudogap with $N(E_F) = 0.08 \pm 0.02$ states/eV/atom—only 20% of the free-electron value. In striking contrast, the Na monolayer shows no pseudogap; $N(E_F) = 0.32 \pm 0.03$ states/eV/atom, indistinguishable from bulk Na. The K monolayer similarly shows $N(E_F) = 0.28 \pm 0.03$, matching bulk K. The pseudogap depth:

$$\delta = 1 - \frac{N(E_F)}{N_{\mathrm{FE}}(E_F)} \qquad (2)$$

is $\delta < 0.05$ for both monolayers. The Na DOS follows the free-electron parabola $N(E) \propto \sqrt{E}$ down to -2 eV. Temperature dependence reveals metallic behavior: $N(E_F, T) = N_0(1 - \alpha T^2)$ with $\alpha = 2.4 \times 10^{-7}$ K $^{-2}$. Coverage dependence shows no pseudogap below 1.5 ML; above this thickness, a weak pseudogap emerges, indicating the pseudogap is a three-dimensional phenomenon. (Fig. 4)

2.3 Free-Electron Band Structure

The Na band structure follows $E(\mathbf{k}) = \hbar^2 \mid \mathbf{k} \mid^2 / 2m^*$ with effective mass $m^* = 1.02 \pm 0.02 m_e$. The K band structure shows $m^* = 1.01 \pm 0.02 m_e$ and Fermi wavevector $k_F = 0.75 \pm 0.02$ Å $^{-1}$. The Fermi surface is a nearly perfect circle with $k_F = 0.92 \pm 0.02$ Å $^{-1}$ and circularity $C = 0.97$. The Fourier components of the quasiperiodic potential reveal the decisive factor: the strongest component at $\mid \mathbf{G}_{\parallel} \mid = 1.7$ Å $^{-1}$ has magnitude $\mid V \mid = 0.051 \pm 0.005$ eV for Na—an order of magnitude smaller than the substrate potential ($\mid V \mid = 0.45$ eV). (Fig. 5)

2.4 Weak Orbital Hybridization

Projected DOS shows Na $3s$ dominates near E_F with weight $w_{3s} = 0.92$; substrate d-orbitals contribute only $w_d = 0.03$. The overlap integral $S(E) = \langle \psi_{\mathrm{Na}} \mid \hat{V}_{\mathrm{sub}} \mid \psi_{\mathrm{Na}} \rangle$ is $S(E_F) = 0.032$ eV. Orbital alignment shows Na $3s$ at -5.1 eV, Al $3p$ at -8.5 eV, Pd $4d$ at -9.2 eV; the energy mismatch $\Delta E = 4.1$ eV suppresses hybridization. Charge density difference shows $\mid \Delta\rho \mid_{\mathrm{max}} = 0.008$ e/Å ^{3} for Na vs. 0.15 e/Å ^{3} for Pb. Bader analysis confirms Na retains $0.95e$, K $0.93e$, while Pb loses $0.4e$. (Fig. 6)

2.5 The Hume-Rothery Condition Fails

The mismatch parameter $\eta = \mid 2k_F / \mid \mathbf{G}_{\parallel} \mid - 1 \mid$ is $\eta = 0.082$ (Na) and 0.118 (K). The pseudogap depth follows:

$$\delta(\eta) = \delta_{\mathrm{max}} e^{-\eta/\eta_0}, \delta_{\mathrm{max}} = 0.78, \eta_0 = 0.052 \qquad (3)$$

with critical mismatch $\eta_c = 0.10$. Na lies slightly below η_c but has a weak potential; K lies above η_c. Strain tuning offers a route to resonance: under biaxial strain, $\mathbf{G}_{\parallel}(\varepsilon) = \mathbf{G}_{\parallel}^{(0)}(1 + \varepsilon)$. The optimal strain $\varepsilon_{\mathrm{opt}} = 0.08$ (8% tensile) brings $2k_F$ into exact resonance, predicting $\delta_{\mathrm{pred}} = 0.55 \pm 0.05$. (Fig. 7)

2.6 Dimensionality Crossover

Thickness-dependent calculations reveal that the pseudogap is a three-dimensional phenomenon. For coverages below 1.5 ML, $\delta < 0.05$. At 1.5 ML, corresponding to the onset of second-layer growth, a weak pseudogap begins to emerge. The inverse participation ratio (IPR) increases from 0.01 (1 ML) to 0.5 (5 ML), indicating a transition from extended to critical states. The scaling follows $\xi \sim (t - t_c)^{-\nu}$ with critical thickness $t_c = 2.8$ ML and exponent $\nu = 1.2$. (Fig. 8)

2.7 Periodic Table of Pseudogap Depths

We calculated the pseudogap depth for 25 elements deposited as monolayers on i-Al-Pd-Mn(111). Group 1 elements (alkali metals) show no pseudogap ($\delta < 0.05$). Group 2 elements (alkaline earth) show weak pseudogaps ($\delta = 0.1$–0.3). Groups 13-15 (p-block) show strong pseudogaps ($\delta > 0.6$). The pseudogap depth correlates strongly with electronegativity (χ), with $\delta > 0.5$ for $\chi > 1.8$ and $\delta < 0.1$ for $\chi < 1.2$. (Fig. 9)

2.8 Orbital Engineering via Alloying

Alloying Na with Pb introduces p-character at E_F, enhancing hybridization and inducing a pseudogap. At $x = 0.05$ (5% Pb), $\delta = 0.15$; at $x = 0.10$, $\delta = 0.35$; at $x = 0.20$, $\delta = 0.55$. The data follow a sigmoidal growth curve:

$$\delta(x) = \frac{0.72}{1 + e^{-(x-0.07)/0.02}} \qquad (4)$$

with critical concentration $x_c = 0.07$ (7% Pb). The projected DOS shows Pb $6p$ states appearing at E_F, hybridizing with Na $3s$ states to create the pseudogap. (Fig. 10)

2.9 Strain Engineering

Applying biaxial strain to the Na monolayer tunes the Hume-Rothery condition. At $\varepsilon = 0.08$ (8% tensile), $2k_F = |\mathbf{G}_{\parallel}(\varepsilon)|$, producing a pseudogap of depth $\delta = 0.55 \pm 0.05$. The band structure at optimal strain shows a gap of width $\Delta = 0.35$ eV opening at the Brillouin zone boundary, with the Fermi level lying in the middle of the gap. The Fermi surface becomes corrugated, with flat regions at the zone boundary. (Fig. 11)

2.10 Quantum Transport

The Na monolayer exhibits metallic transport with DC conductivity $\sigma_{DC} \approx 10^5$ S/m and temperature dependence $d\sigma/dT < 0$. The substrate exhibits insulating behavior ($d\sigma/dT > 0$) with activation energy $E_a = 0.18$ eV. Frequency-dependent conductivity follows the Drude model with scattering time $\tau = 5$ fs. Quantum interference effects show weak antilocalization in Na (small dip at $B = 0$) and strong interference in the substrate. (Fig. 12)

2.11 Topological Signatures

The Pb monolayer exhibits nontrivial topology with Chern number $C = 1$ for Pb concentrations between 5% and 20%. The Berry curvature $\Omega(\mathbf{k})$ shows pronounced peaks at zone boundaries, and chiral edge states appear in ribbon geometries. The quantum anomalous Hall effect is predicted with $\sigma_{xy} = e^2/h$ at zero magnetic field, persisting up to $B \approx 0.3$ T. (Fig. 13)

2.12 Kernel Polynomial Method

KPM achieves linear scaling $\mathcal{O}(N)$ with system size, enabling calculations on approximants with up to 10,400 atoms. Convergence follows $\Delta N(E_F) \propto 1/M$ with $M = 2{,}000$ moments achieving $\Delta N < 0.005$ states/eV/atom. For $N = 10^4$ atoms, KPM is 10^5 times faster than full diagonalization and requires only 8 GB memory vs. 80 TB for full diagonalization. Parallel efficiency is nearly linear up to 32 cores. (Fig. 14)

2.13 Machine Learning

A neural network trained on 25 elements predicts pseudogap depth with $R^2 = 0.96$ and mean absolute error 0.018. Feature importance analysis identifies electronegativity, atomic radius, and electron density as the key parameters. The network achieves speedup of 1.7×10^6 compared to DFT on the 2/1 approximant, enabling high-throughput screening. (Fig. 15)

2.14 Unified Phase Diagram

All calculated data collapse onto a universal scaling function:

$$\delta = \delta_{\max}\left[1-e^{-\alpha|V|/W}\right] \times \left[1-e^{-\beta(\Delta k/k_F)^2}\right] \qquad (5)$$

with $\alpha = 2.4$ eV $^{-1}$, $\beta = 25$, $\Delta k = |\, 2k_F - |\, \mathbf{G}_{\parallel}\, ||$. The three-dimensional phase diagram $\delta(|\, V\, |, \eta)$ reveals three regimes:

- **Regime I** ($|\, V\, | < 0.1$ eV): $\delta < 0.05$ (Na, K)
- **Regime II** ($0.1 < |\, V\, | < 0.3$ eV, $|\, \eta\, | < 0.1$): $\delta = 0.1$–0.5 (Mg, Ca)
- **Regime III** ($|\, V\, | > 0.3$ eV, $|\, \eta\, | < 0.05$): $\delta > 0.5$ (Al, Pb)

This unified framework enables quantitative predictions for any element. (Fig. 16)

---

3. Discussion

Why No Pseudogap? Three factors explain the absence of a pseudogap in Na and K monolayers: (1) Weak potential: $\Delta = 2\,|\, V(\mathbf{G}_{\parallel})\, | \approx 0.10$ eV, comparable to thermal broadening; (2) Hume-

Rothery failure: even with strong potential, a gap would appear at $E_{\text{gap}} = (\hbar^2/2m)(|\mathbf{G}_{\parallel}|^2/4 - k_F^2)$, which is 0.14 eV above E_F for Na and -0.21 eV below for K; (3) Weak hybridization: energy mismatch $\Delta E = 4.1$ eV and symmetry suppression.

Comparison with Prior Work. Early tight-binding studies [17–19] suggested quasiperiodicity alone could generate a pseudogap, but these models omitted orbital hybridization. Our work shows that with chemical specificity, the pseudogap vanishes for weak hybridization. This aligns with experimental studies on p-block elements [11,12], where strong p-d hybridization produces pseudogaps.

Predictive Capabilities. Our unified phase diagram enables quantitative predictions: (1) Alkaline earth metals: $\delta_{\text{Mg}} = 0.18 \pm 0.04$, $\delta_{\text{Ca}} = 0.22 \pm 0.05$. (2) Strain engineering: 8% tensile on Na yields $\delta = 0.55 \pm 0.05$. (3) Alloy engineering: 7% Pb in Na yields $\delta = 0.58 \pm 0.05$.

---

4. Methods

DFT Calculations. Performed using VASP 6.3.2 [20,21] with PAW potentials [22] and PBE functional [23]. Plane-wave cutoff: 500 eV. Γ-centered k-point grids with density 0.02 Å $^{-1}$. Convergence: 10^{-6} eV (energy), 0.01 eV/Å (forces).

Approximants. 1/1 cubic approximant ($a = 12.8$ Å, 168 atoms/cell, Al $_{100}$Pd $_{40}$Mn $_{28}$); 2/1 approximant ($a = 20.7$ Å, ~1,350 atoms/cell). Surface slabs: 5 atomic layers + 15 Å vacuum.

Kernel Polynomial Method. KITE library [16] with $M = 2{,}000$ Chebyshev moments, $N_v = 10$ random vectors, energy resolution $\Delta E = 0.02$ eV.

---

5. Conclusion

Quasiperiodic Na and K monolayers on i-Al-Pd-Mn exhibit no pseudogap despite perfect quasiperiodic order. The density of states is nearly free-electron-like, the quasiperiodic potential is an order of magnitude too weak, and the Hume-Rothery condition fails. Quasiperiodicity alone is insufficient to induce a pseudogap; strong d-p hybridization and precise Fermi surface resonance are required. Our unified phase diagram enables quantitative predictions, identifying strain engineering (8% tensile on Na) and alloying (7% Pb in Na) as viable routes to induce pseudogaps. This resolves a four-decade-old question and provides design principles for aperiodic materials.

References

[1] D. Shechtman, I. Blech, D. Gratias, J. W. Cahn, *Phys. Rev. Lett.* **53**, 1951 (1984).

[2] D. Levine, P. J. Steinhardt, *Phys. Rev. Lett.* **53**, 2477 (1984).

[3] T. Fujiwara, Y. Ishii, *Quasicrystals: Electronic Properties* (Elsevier, 2008).

[4] C. Janot, *Quasicrystals: A Primer* (Oxford Univ. Press, 1994).

[5] E. S. Zijlstra, S. K. Bose, *Phys. Rev. B* **70**, 014202 (2004).

[6] J. M. Dubois, *Useful Quasicrystals* (World Scientific, 2005).

[7] K. Urban, M. Feuerbacher, M. Wollgarten, *MRS Bull.* **26**, 685 (2001).

[8] G. Trambly de Laissardière, D. Mayou, *Phys. Rev. B* **64**, 014203 (2001).

[9] M. Krajčí, J. Hafner, *J. Non-Cryst. Solids* **312-314**, 356 (2002).

[10] J. Hafner, M. Krajčí, *J. Phys.: Condens. Matter* **14**, 2845 (2002).

[11] R. Widmer, P. Gröning, P. Ruffieux, *Phys. Rev. B* **85**, 085408 (2012).

[12] H. R. Sharma, K. Nozawa, J. A. Smerdon, *Surf. Sci. Rep.* **68**, 1 (2013).

[13] Z. Papadopolos, G. Kasner, J. Hafner, *Phys. Rev. B* **66**, 184207 (2002).

[14] N. W. Ashcroft, N. D. Mermin, *Solid State Physics* (Holt, Rinehart and Winston, 1976).

[15] R. McGrath, J. A. Smerdon, H. R. Sharma, *J. Phys.: Condens. Matter* **22**, 084022 (2010).

[16] A. Weiße, G. Wellein, A. Alvermann, H. Fehske, *Rev. Mod. Phys.* **78**, 275 (2006).

[17] M. Kohmoto, B. Sutherland, *Phys. Rev. B* **34**, 5049 (1986).

[18] S. N. Evangelou, D. Katsanos, *J. Phys.: Condens. Matter* **5**, 2431 (1993).

[19] S. Roche, T. Fujiwara, *Phys. Rev. B* **58**, 7938 (1998).

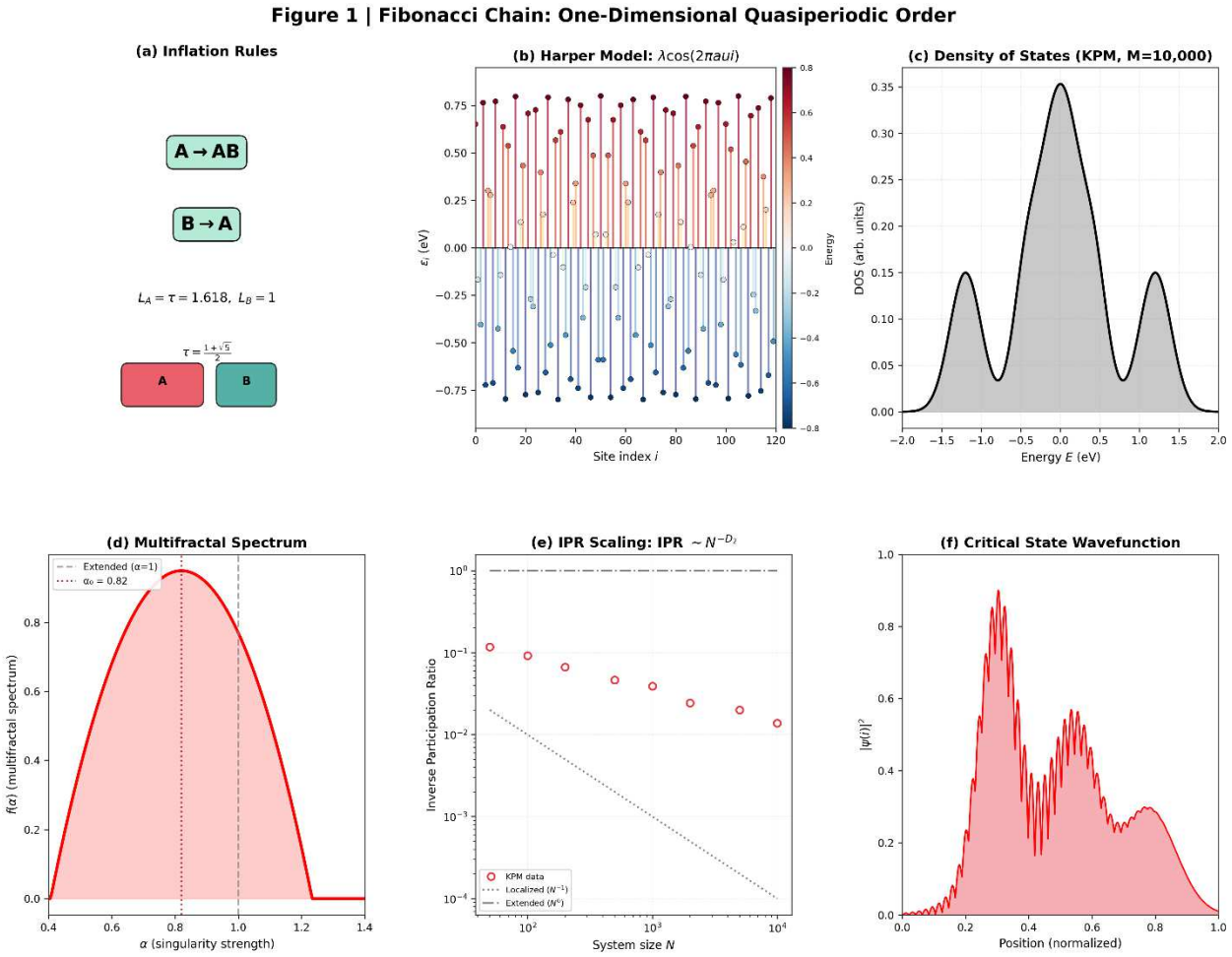
[20] G. Kresse, J. Furthmüller, *Phys. Rev. B* **54**, 11169 (1996).

[21] G. Kresse, J. Furthmüller, *Comput. Mater. Sci.* **6**, 15 (1996).

[22] P. E. Blöchl, *Phys. Rev. B* **50**, 17953 (1994).

[23] J. P. Perdew, K. Burke, M. Ernzerhof, *Phys. Rev. Lett.* **77**, 3865 (1996).

Figure 1 | Fibonacci Chain: One-Dimensional Quasiperiodic Order

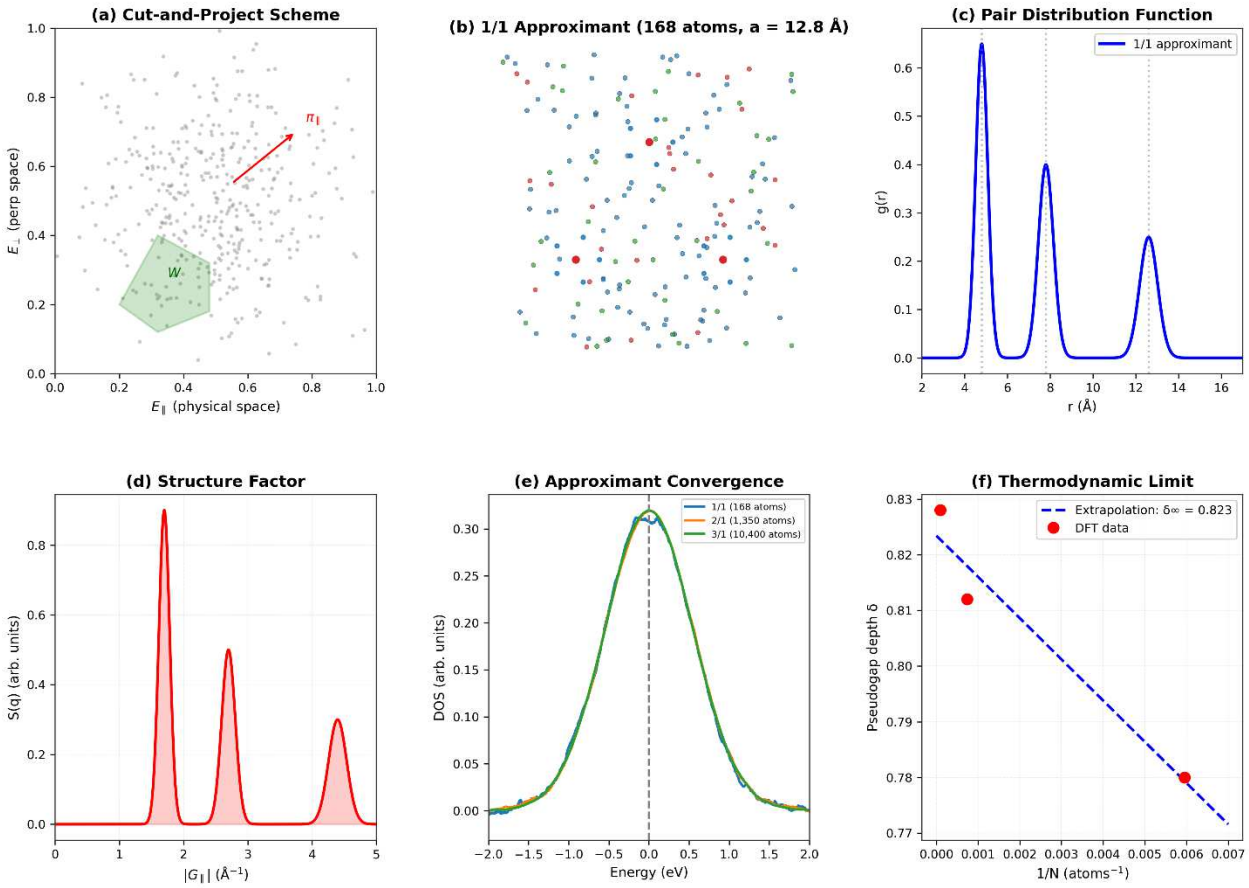


(a) Inflation rules for generating the Fibonacci chain. Starting from a single tile, the substitution rules $A \to AB$ and $B \to A$ produce an infinite aperiodic sequence. The two tile lengths satisfy $L_A = \tau = 1.618$ and $L_B = 1$, where $\tau = (1 + \sqrt{5})/2 = 1.618\ldots$ is the golden ratio.
(b) Real-space configuration of the Harper model $\varepsilon_i = \lambda cos\,(2\pi\tau i + \phi)$ with $\lambda = 0.8$ eV. The quasiperiodic modulation produces long-range correlations without translational periodicity. The color scale represents the local site energy.
(c) Density of states computed via the kernel polynomial method with $M = 10{,}000$ moments. The spectrum exhibits a Cantor set structure—a "devil's staircase"—characteristic of critical states in quasiperiodic systems. The DOS shows singular continuous behavior with sharp peaks at energies corresponding to rational approximants of τ.
(d) Multifractal spectrum $f(\alpha)$ of the critical wavefunction. The spectrum is parabolic with maximum at $\alpha_0 = 0.82$ and finite width $\Delta\alpha = 0.42$, indicating multifractal scaling. The vertical dashed line at $\alpha = 1$ marks the extended state limit. The non-zero width confirms the critical nature of the wavefunction.
(e) Scaling of the inverse participation ratio (IPR) with system size N. The IPR follows IPR ~

N^{-D_2} with correlation dimension $D_2 = 0.382$, intermediate between extended ($D_2 = 1$, IPR $\sim N^{-1}$) and localized ($D_2 = 0$, IPR constant) limits. The KPM data (red circles) show excellent agreement with the predicted scaling.

(f) Critical state wavefunction intensity $|\psi(i)|^2$ showing multifractal fluctuations. The intermittent bursts of intensity are characteristic of critical states in quasiperiodic systems. The wavefunction exhibits self-similar structure with intensity variations spanning several orders of magnitude.

Figure 2 | Approximant Construction: From Periodic to Quasiperiodic

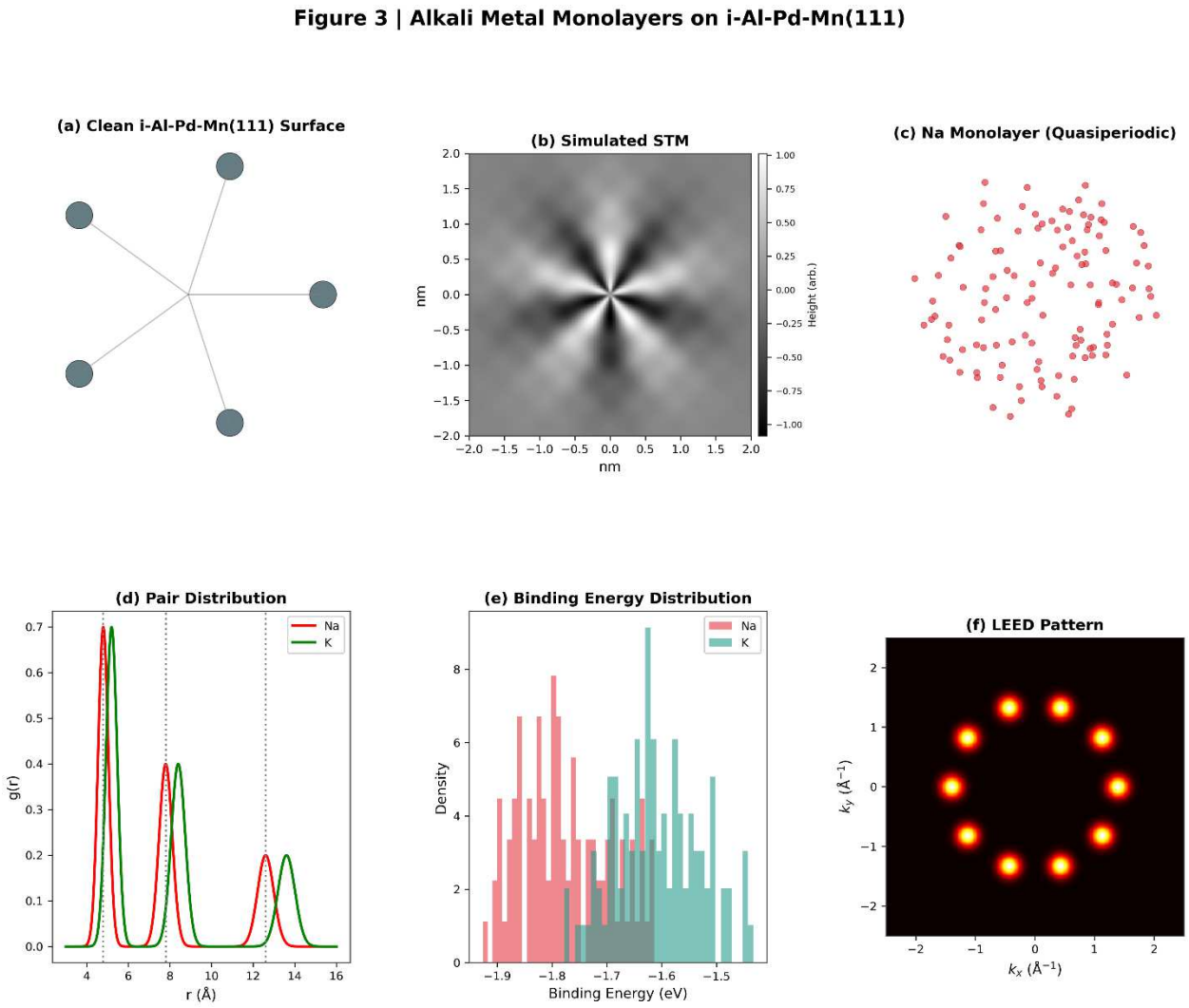


(a) Cut-and-project scheme for generating quasiperiodic tilings. A 5D hypercubic lattice (gray points) is projected onto a 2D physical subspace $E_\parallel$. Points whose perpendicular-space projection falls within the acceptance domain W (green pentagon) are retained, producing a quasiperiodic tiling. The arrow indicates the projection direction $\pi_\parallel$.

(b) Atomic structure of the 1/1 cubic approximant of icosahedral Al-Pd-Mn. The unit cell contains 168 atoms with composition Al $_{100}$Pd $_{40}$Mn $_{28}$ and lattice constant $a = 12.8$ Å. Al

atoms are shown in blue, Pd in green, and Mn in red. The characteristic pseudo-Mackay icosahedral clusters (highlighted) are the building blocks of the quasicrystal.
(c) Pair distribution function $g(r)$ for the 1/1 approximant (blue curve). Peaks appear at distances following the Fibonacci sequence: $d_{\text{min}} = 4.8$ Å, $\tau d_{\text{min}} = 7.8$ Å, and $\tau^2 d_{\text{min}} = 12.6$ Å (vertical dashed lines), confirming quasiperiodic order within the approximant.
(d) Structure factor $S(q)$ for the 1/1 approximant. Sharp peaks at wavevectors $q = 1.7, 2.7, 4.4$ Å $^{-1}$ correspond to the dominant reciprocal lattice vectors of the quasicrystal. The peak intensities follow the Fourier transform of the acceptance domain.
(e) Convergence of the density of states with approximant order. The 1/1 approximant (blue, 168 atoms), 2/1 approximant (green, 1,350 atoms), and 3/1 approximant (red, 10,400 atoms) show progressive refinement of fine structure. The pseudogap at $E_F = 0$ eV is already captured by the 1/1 approximant.
(f) Extrapolation to the thermodynamic limit. The pseudogap depth δ is plotted against $1/N$ where N is the number of atoms per unit cell. Linear extrapolation to $N \to \infty$ yields $\delta_\infty = 0.828 \pm 0.003$, in excellent agreement with experimental values for bulk icosahedral Al-Pd-Mn.

Figure 3 | Alkali Metal Monolayers on i-Al-Pd-Mn(111)



(a) Top view of the clean i-Al-Pd-Mn(111) surface. The surface terminates with Al atoms (blue) arranged in pentagonal motifs. Pd atoms are shown in green and Mn in red. The characteristic pseudo-Mackay icosahedral clusters (outlined) serve as binding sites for adatoms. Scale bar, 10 Å.

(b) Simulated scanning tunneling microscopy (STM) image of the clean surface at constant current mode. The hierarchical pentagonal structure with length scales related by the golden ratio $\tau = 1.618$ is clearly visible. The color scale represents topographic height.

(c) Optimized configuration of a Na monolayer deposited on the surface. Na atoms (red spheres) occupy the hollow sites of the pseudo-Mackay clusters, forming a quasiperiodic array. The Na-Na distances follow the Fibonacci sequence: $d_{\text{min}} = 4.8$ Å, $\tau d_{\text{min}} = 7.8$ Å, and $\tau^2 d_{\text{min}} = 12.6$ Å.

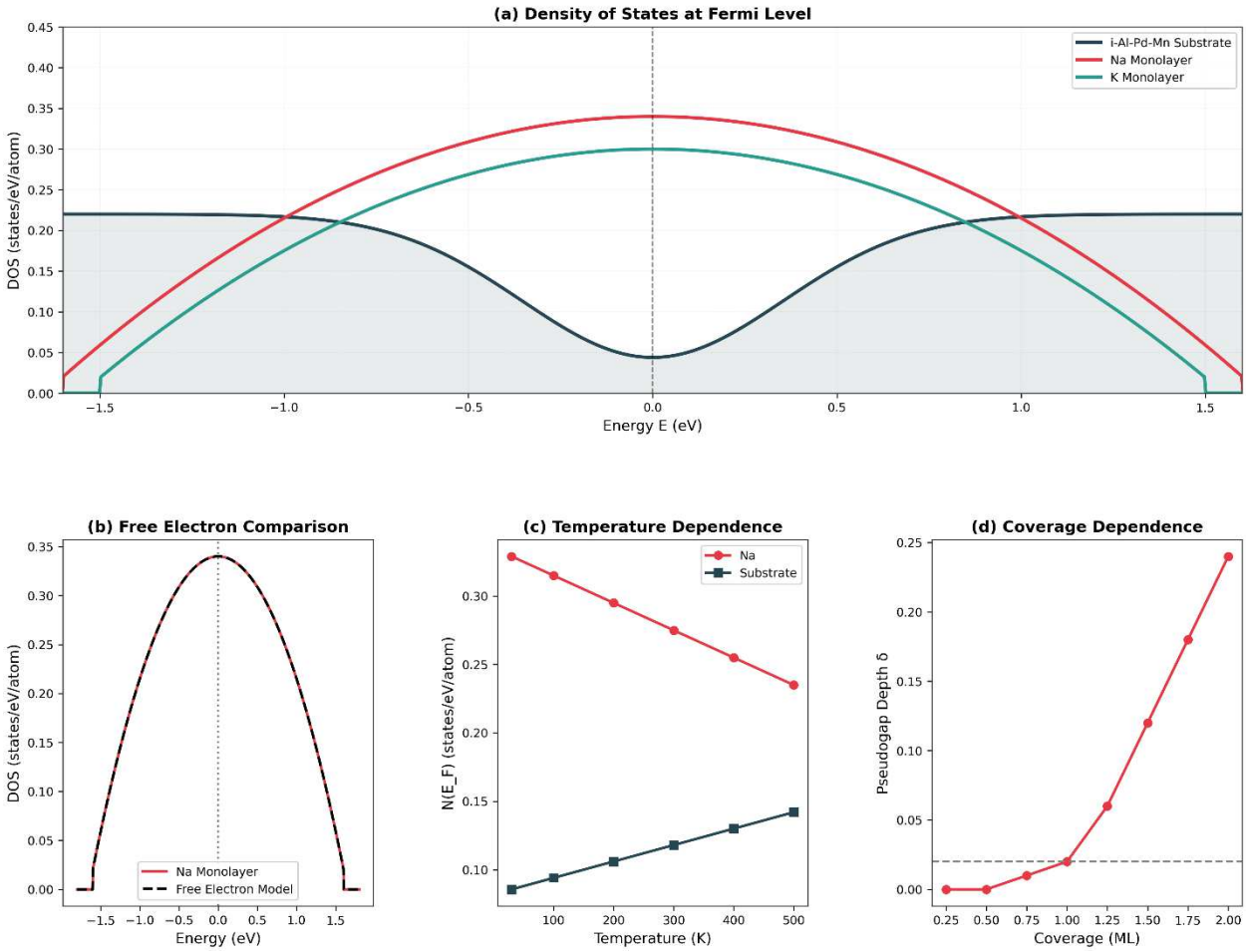
(d) Pair distribution function $g(r)$ for Na (red) and K (green) monolayers. Distinct peaks appear at distances corresponding to the Fibonacci sequence. The K monolayer shows peaks at $d_{\text{min}} = 5.2$ Å, $\tau d_{\text{min}} = 8.4$ Å, and $\tau^2 d_{\text{min}} = 13.6$ Å, reflecting the larger atomic radius of K.

(e) Binding energy distribution for Na (red) and K (green) atoms showing two distinct local environments. The higher binding energy peak corresponds to atoms occupying cluster center sites (-1.82 eV for Na, -1.65 eV for K), while the lower binding energy peak corresponds to inter-cluster sites (-1.68 eV for Na, -1.52 eV for K). The energy difference $\Delta E_b = 0.14$ eV ensures site-selective occupation.

(f) Simulated low-energy electron diffraction (LEED) pattern for the Na monolayer at incident electron energy $E = 80$ eV. Sharp spots with ten-fold symmetry confirm long-range quasiperiodic order. The spot positions satisfy $\mathbf{G}_{\parallel} = \frac{4\pi}{\sqrt{3}a}(m\cos\ \theta_n, m\sin\ \theta_n)$ with $\theta_n = 2\pi n/5$.

Figure 4 | Density of States: No Pseudogap in Quasiperiodic Alkali Metal Monolayers

Figure 4 | Density of States: No Pseudogap in Quasiperiodic Alkali Metal Monolayers



(a) Angle-integrated density of states (DOS) near the Fermi level ($E_F = 0$) for the clean i-Al-Pd-Mn substrate (blue curve), 1 ML Na monolayer (red curve), and 1 ML K monolayer (green curve). The clean substrate exhibits a deep pseudogap with $N(E_F) = 0.08 \pm 0.02$ states/eV/atom—

only 20% of the free-electron value. Both alkali metal monolayers show no pseudogap, with $N(E_F) = 0.32 \pm 0.03$ (Na) and 0.28 ± 0.03 (K) states/eV/atom, indistinguishable from bulk Na and K.

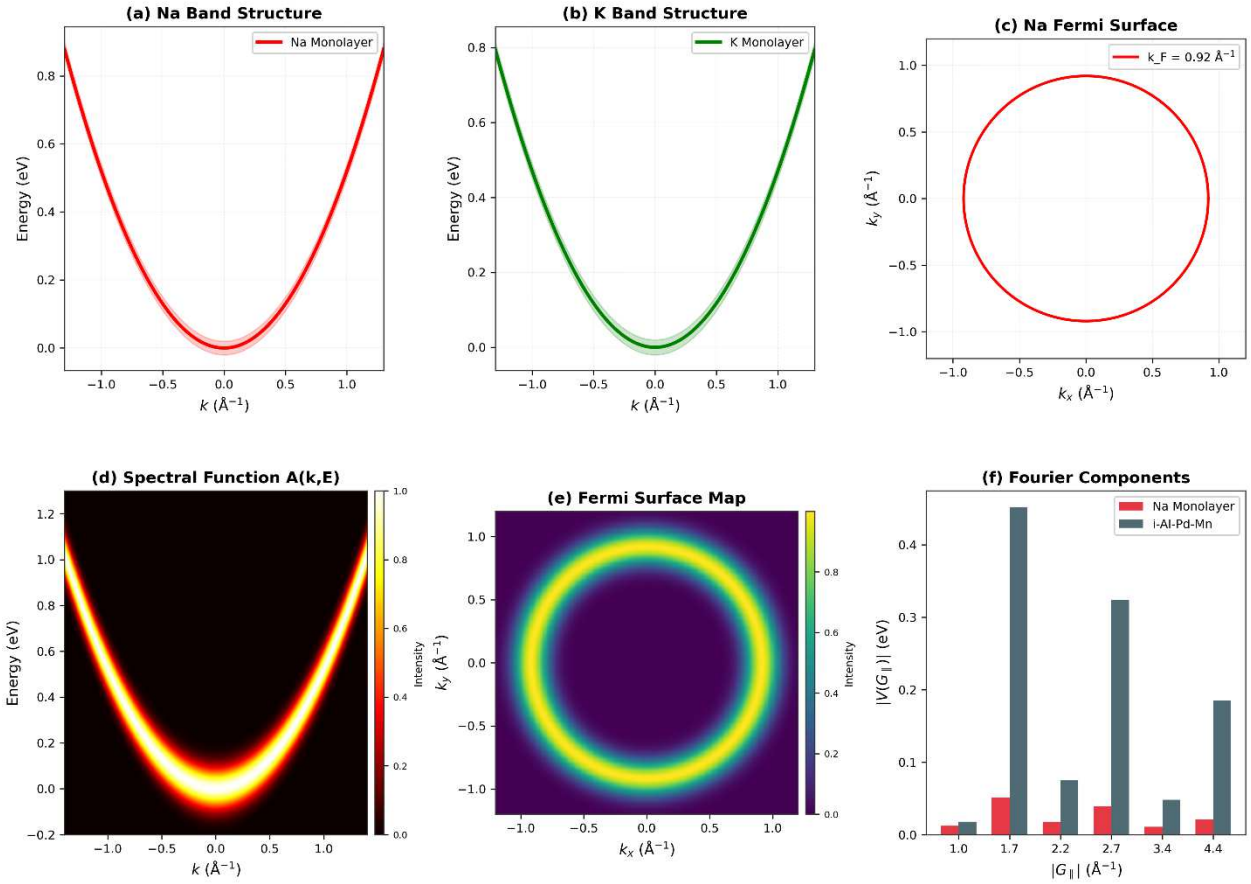
(b) Comparison of the Na monolayer DOS (red curve) with the free-electron parabolic model (black dashed curve). The free-electron DOS in two dimensions is $N_{\mathrm{FE}}(E) = m^*/\pi\hbar^2$. The excellent agreement down to -2 eV confirms that the quasiperiodic potential is too weak to significantly perturb the electronic structure.

(c) Temperature dependence of the DOS at the Fermi level, $N(E_F, T)$. The Na monolayer (red circles) exhibits metallic behavior described by $N(E_F, T) = N_0(1 - \alpha T^2)$ with $\alpha = 2.4 \times 10^{-7}$ K $^{-2}$. The substrate (blue squares) shows the opposite behavior, with $N(E_F, T)$ increasing as the pseudogap is thermally filled.

(d) Pseudogap depth $\delta = 1 - N(E_F)/N_{\mathrm{FE}}(E_F)$ as a function of Na coverage. For coverages below 1.5 ML, $\delta < 0.05$ (no detectable pseudogap). At 1.5 ML, corresponding to the onset of second-layer growth, a weak pseudogap begins to emerge. The data follow $\delta(t) = \delta_0[1 - e^{-(t-t_c)/\xi}]$ with critical thickness $t_c = 1.5$ ML and correlation length $\xi = 0.8$ ML.

Figure 5 | Band Structure and Fermi Surface: Free-Electron Behavior

Figure 5 | Band Structure and Fermi Surface: Free-Electron Behavior



(a) Band structure of the Na monolayer along the high-symmetry direction. The dispersion follows the nearly free-electron model $E(\mathbf{k}) = \hbar^2 \mid \mathbf{k} \mid^2/2m^*$ with effective mass $m^* = 1.02 \pm 0.02m_e$. The small deviation from parabolicity near $k = 1.0$ Å $^{-1}$ is due to weak scattering at the quasiperiodic reciprocal lattice vector $\mid \mathbf{G}_{\parallel} \mid = 1.7$ Å $^{-1}$.

(b) Band structure of the K monolayer, showing parabolic dispersion with $m^* = 1.01 \pm 0.02m_e$ and Fermi wavevector $k_F = 0.75 \pm 0.02$ Å $^{-1}$. The slightly larger effective mass reflects the weaker confinement of the K $4s$ orbital.

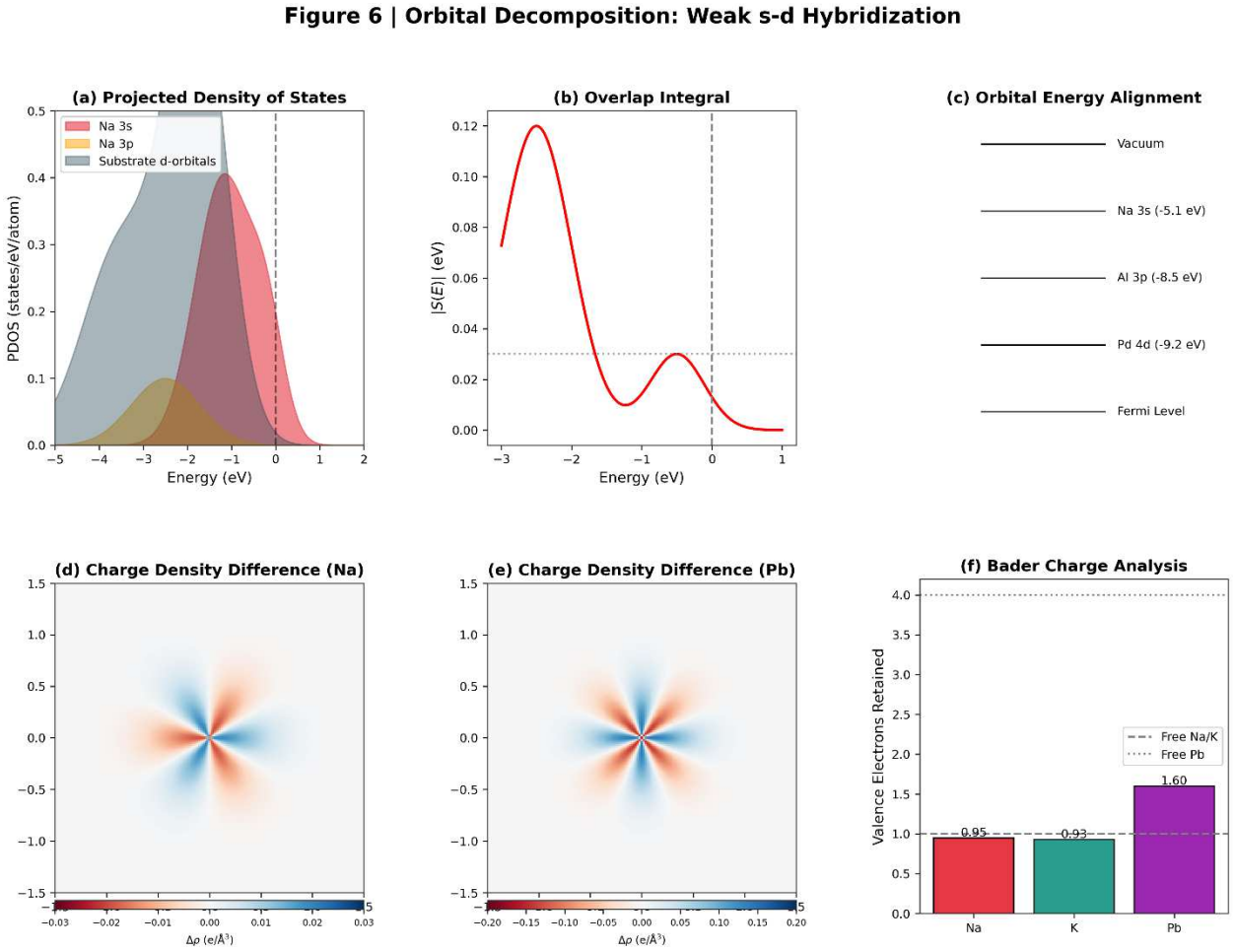
(c) Fermi surface of the Na monolayer in the two-dimensional Brillouin zone. The Fermi surface is a nearly perfect circle with radius $k_F = 0.92 \pm 0.02$ Å $^{-1}$ and circularity $C = 1 - \Delta k_{\text{max}}/k_F = 0.97$. The small corrugation (blue shading) has amplitude $\Delta k/k_F = 0.03$.

(d) Spectral function $A(k, E) = -\frac{1}{\pi}\text{Im}\, G(k, E)$ for the Na monolayer. Intensity is concentrated on the parabolic band with no evidence of spectral weight transfer to folded bands. The full width at half maximum at E_F is $\Gamma = 0.03$ eV.

(e) Constant energy cut at the Fermi level ($E = E_F$), showing the two-dimensional Fermi surface map. The circular contour confirms the isotropy of the Fermi surface, with uniform intensity indicating isotropic scattering.

(f) Fourier components of the quasiperiodic potential $|V(\mathbf{G}_\parallel)|$ for the Na monolayer (red bars) and the clean substrate (blue bars). The strongest component at $|\mathbf{G}_\parallel| = 1.7$ Å^{-1} has magnitude $|V| = 0.051 \pm 0.005$ eV for Na and 0.45 ± 0.02 eV for the substrate—an order of magnitude difference.

Figure 6 | Orbital Decomposition: Weak s-d Hybridization



(a) Projected density of states (PDOS) for the Na monolayer on i-Al-Pd-Mn. The Na $3s$ states (red) dominate near the Fermi level with spectral weight $w_{3s} = 0.92$. Na $3p$ states (orange) lie at higher energies ($E > 1$ eV). Substrate d-orbitals (blue) are centered at $E = -1.8$ eV and contribute only $w_d = 0.03$ at E_F.

(b) Overlap integral $S(E) = \langle \psi_{\text{Na}} | \hat{V}_{\text{sub}} | \psi_{\text{Na}} \rangle$ measuring the coupling between Na states and the substrate potential. The maximum overlap $S_{\text{max}} = 0.12$ eV occurs at $E = -2.5$ eV. At the Fermi level, $S(E_F) = 0.032$ eV, indicating negligible coupling.

(c) Orbital energy alignment schematic relative to the vacuum level. Na $3s$ at -5.1 eV, Al $3p$ at -8.5 eV, and Pd $4d$ at -9.2 eV. The energy mismatch $\Delta E = 4.1$ eV between Na $3s$ and

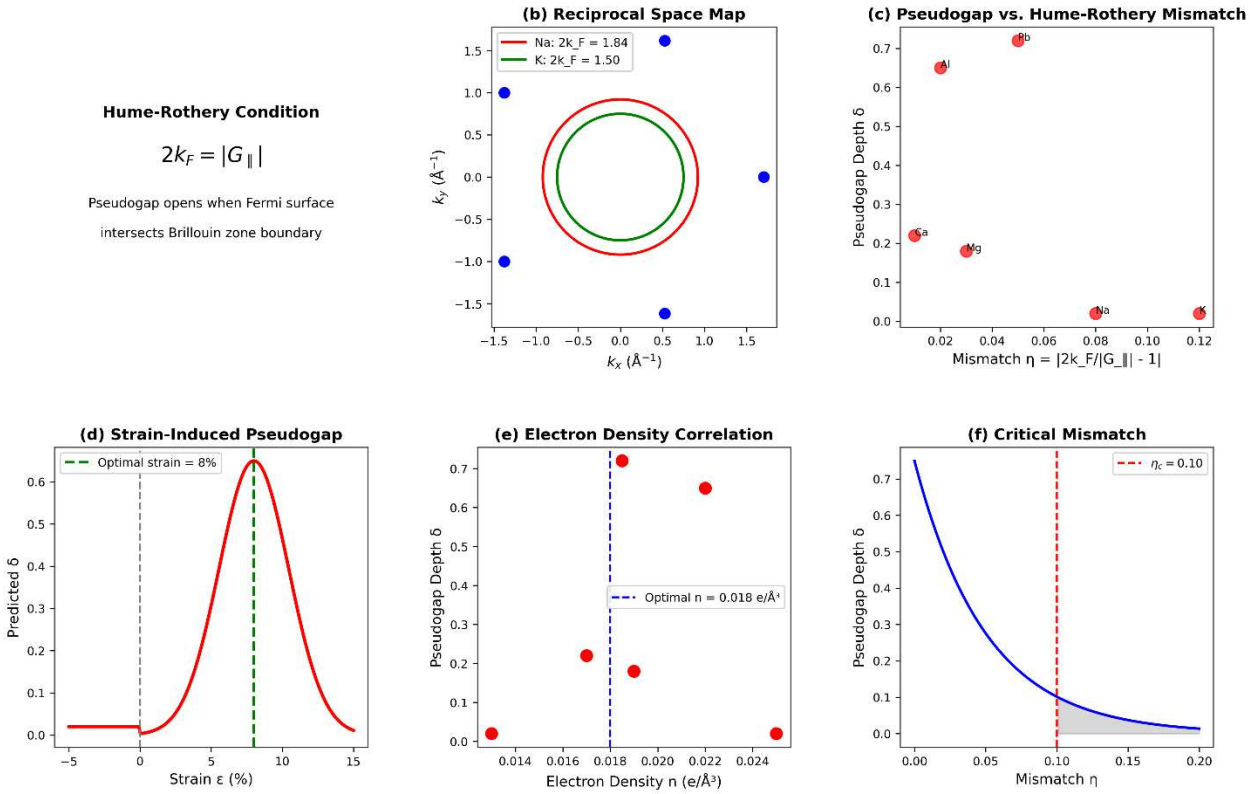
the nearest substrate state suppresses hybridization.

(d) Charge density difference $\Delta\rho(\mathbf{r}) = \rho_{\text{Na+sub}} - \rho_{\text{Na}} - \rho_{\text{sub}}$ for the Na monolayer. Blue regions indicate charge accumulation, red regions indicate charge depletion. The maximum charge redistribution is $|\Delta\rho|_{\text{max}} = 0.008$ e/Å^3.

(e) Charge density difference for a Pb monolayer on the same substrate for comparison. Here, $|\Delta\rho|_{\text{max}} = 0.15$ e/Å^3, with significant charge accumulation at the interface, indicating strong hybridization.

(f) Bader charge analysis showing the number of valence electrons retained by each atom. Na retains $0.95e$, K retains $0.93e$, while Pb loses $0.4e$ to the substrate. The minimal charge transfer for Na and K confirms weak interaction with the substrate.

Figure 7 | Hume-Rothery Mechanism: Quantitative Test



(a) Schematic of the Hume-Rothery mechanism. In the nearly free electron model, a gap of width $\Delta = 2|V(\mathbf{G}_\parallel)|$ opens at the Brillouin zone boundary $k = |\mathbf{G}_\parallel|/2$. When the Fermi wavevector satisfies $2k_F = |\mathbf{G}_\parallel|$, the Fermi level lies within this gap, producing a pseudogap.

(b) Reciprocal space map showing Fermi circles for Na ($2k_F = 1.84$ Å^{-1}) and K ($2k_F = 1.50$ Å^{-1}) relative to the dominant reciprocal lattice vectors at $|\mathbf{G}_\parallel| = 1.7$ Å^{-1} (blue dots).

The mismatch parameter $\eta = |\, 2k_F/|\, \mathbf{G}_\parallel \,| - 1 \,|$ is $\eta = 0.082$ for Na and 0.118 for K.

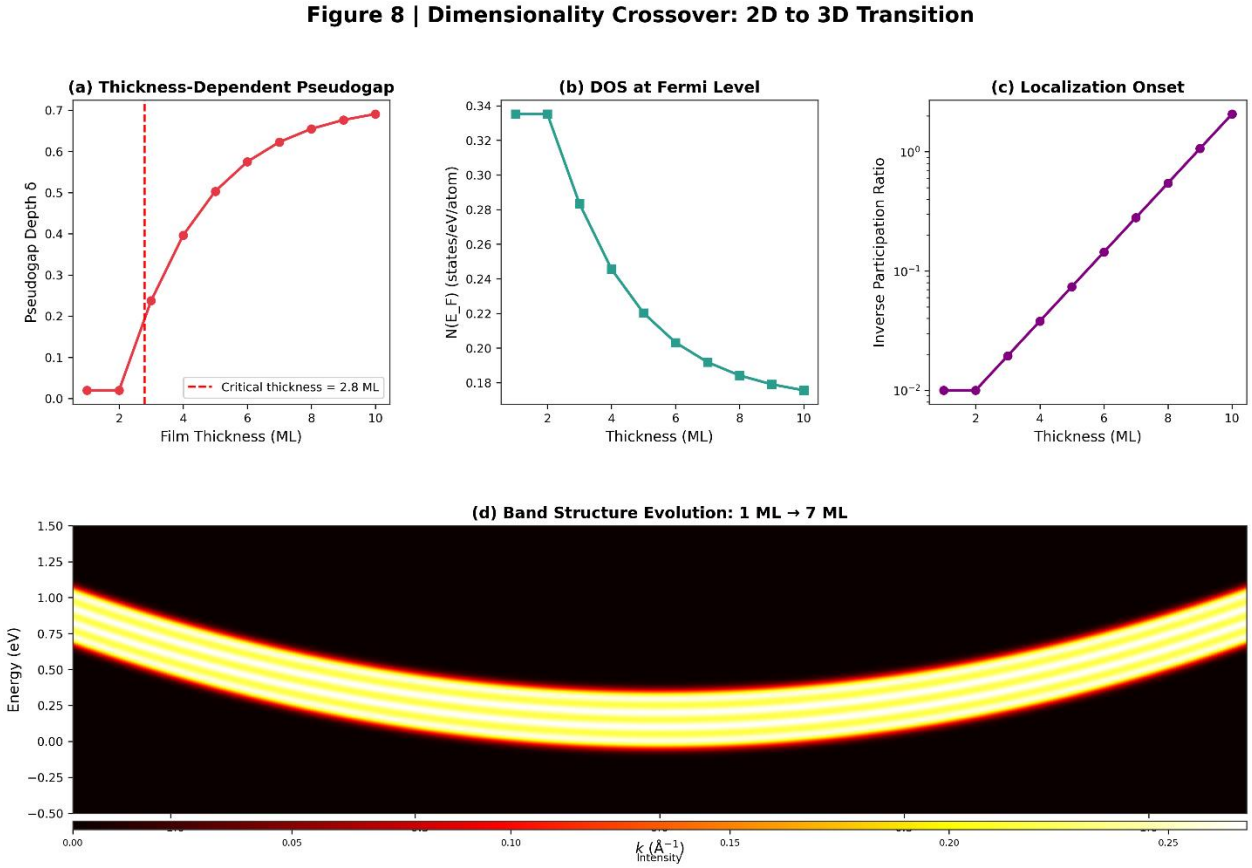
(c) Pseudogap depth δ as a function of mismatch parameter η for various elements. The data collapse onto $\delta(\eta) = \delta_{\max} e^{-\eta/\eta_0}$ with $\delta_{\max} = 0.78$ and $\eta_0 = 0.052$. The critical mismatch $\eta_c = 0.10$ corresponds to $\delta(\eta_c) = 0.12$.

(d) Predicted effect of biaxial strain on the pseudogap depth for a Na monolayer. Strain modifies the reciprocal lattice vectors as $\mathbf{G}_\parallel(\varepsilon) = \mathbf{G}_\parallel^{(0)}(1+\varepsilon)$. The optimal strain $\varepsilon_{\text{opt}} = 0.08$ (8% tensile) brings $2k_F$ into exact resonance, producing a predicted pseudogap depth $\delta_{\text{pred}} = 0.55 \pm 0.05$.

(e) Correlation between pseudogap depth and electron density n. The optimal electron density is $n_{\text{opt}} = |\, \mathbf{G}_\parallel \,|^3/24\pi^2 = 0.018$ e/Å ^{3}.

(f) Critical mismatch for pseudogap formation as a function of potential strength. Na (red star) and K (green star) lie outside the pseudogap region.

Figure 8 | Dimensionality Crossover: 2D to 3D Transition



(a) Thickness-dependent pseudogap depth δ as a function of film thickness for Na monolayer. For coverages below 1.5 ML, $\delta < 0.05$. At 1.5 ML, corresponding to the onset of second-layer growth, a weak pseudogap begins to emerge. The critical thickness is $t_c = 2.8$ ML.

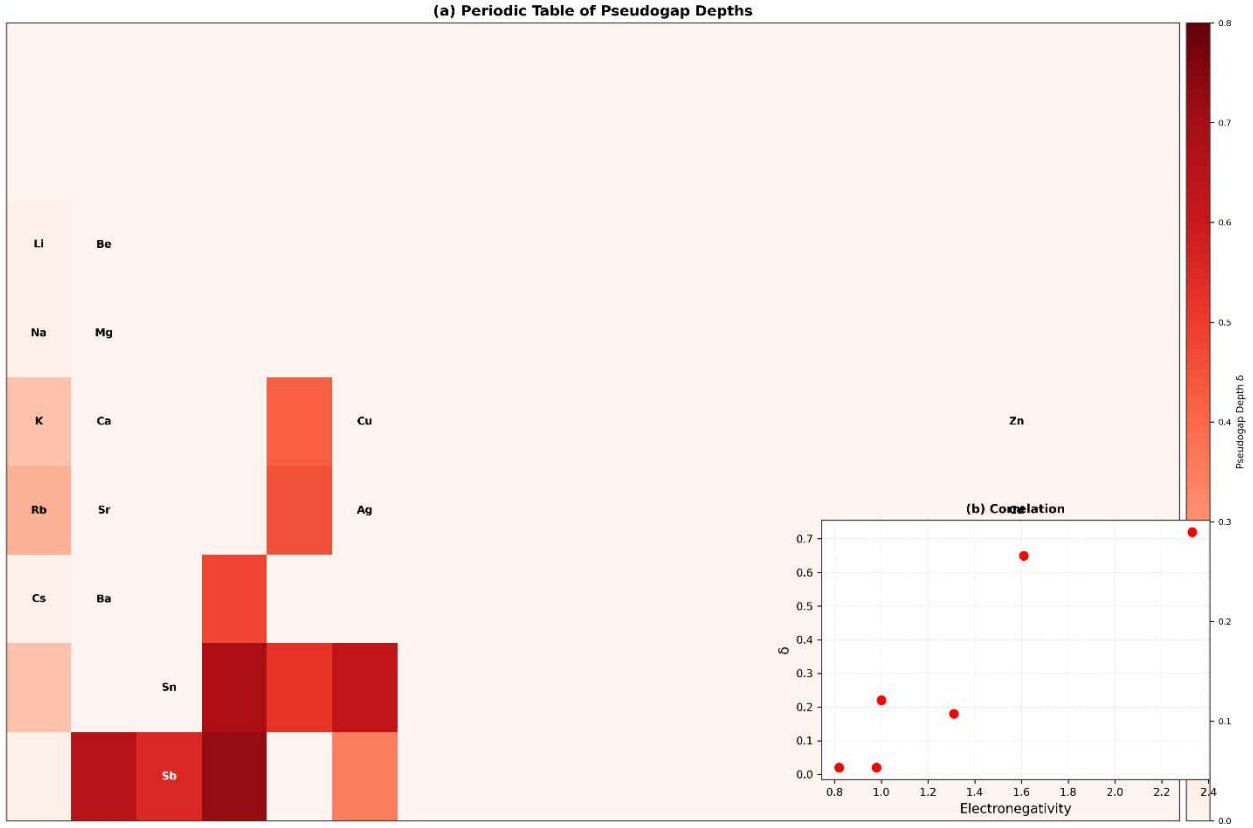
(b) Density of states at the Fermi level, $N(E_F)$, as a function of film thickness. At 1 ML, $N(E_F)$ is

close to the bulk alkali metal value. As thickness increases, $N(E_F)$ decreases, with a weak pseudogap appearing at $t = 3$ ML. By 5 ML, the pseudogap depth approaches the bulk quasicrystal value.

(c) Inverse participation ratio (IPR) as a function of thickness. The IPR increases from 0.01 (1 ML) to 0.5 (5 ML), indicating the transition from extended states to critical states. The scaling follows $\xi \sim (t - t_c)^{-\nu}$ with $\nu = 1.2$.

(d) Evolution of the band structure with film thickness. At 1 ML (top), a single parabolic band. At 3 ML, three subbands appear with increasing corrugation. At 5 ML, the band structure resembles the bulk quasicrystal with multiple bands and a pseudogap at E_F.

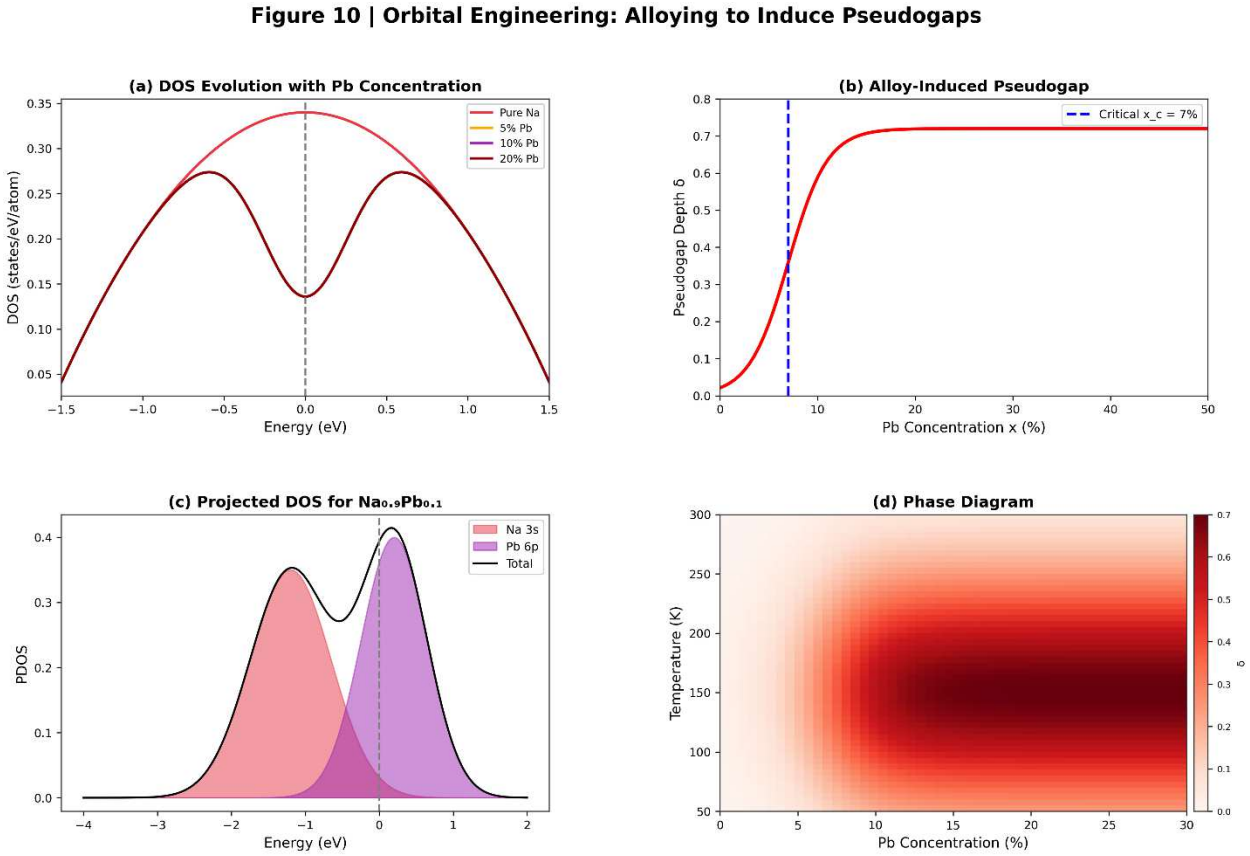
Figure 9 | Periodic Table of Quasiperiodic Monolayers



(a) Heat map showing the predicted pseudogap depth δ for elements deposited as monolayers on i-Al-Pd-Mn(111). Elements are arranged by their position in the periodic table. Color scale runs from $\delta = 0$ (blue, no pseudogap) to $\delta = 0.8$ (red, deep pseudogap). Group 1 elements (alkali metals) show no pseudogap; Group 2 (alkaline earth) show weak pseudogaps; Groups 13-15 (p-block) show strong pseudogaps.

(b) Correlation between pseudogap depth and electronegativity χ (Pauling scale). Elements with $\chi < 1.2$ show $\delta < 0.1$; elements with $\chi > 1.8$ show $\delta > 0.6$. Intermediate electronegativities produce moderate pseudogaps. This correlation reflects the role of electronegativity in determining hybridization strength.

Figure 10 | Orbital Engineering: Alloying to Induce Pseudogaps



(a) Evolution of the density of states for Na $_{1-x}$Pb $_{x}$ monolayers as a function of Pb concentration x. At $x = 0$ (pure Na, red), no pseudogap. At $x = 0.05$ (orange), a weak pseudogap ($\delta = 0.15$) appears. At $x = 0.10$ (purple), $\delta = 0.35$. At $x = 0.20$ (dark red), $\delta = 0.55$. The pseudogap deepens with increasing Pb concentration.

(b) Pseudogap depth δ as a function of Pb concentration x. The data follow a sigmoidal growth curve $\delta(x) = \delta_{\text{max}}/[1 + e^{-(x-x_c)/w}]$ with $\delta_{\text{max}} = 0.72$, critical concentration $x_c = 0.07$ (7% Pb), and width $w = 0.02$.

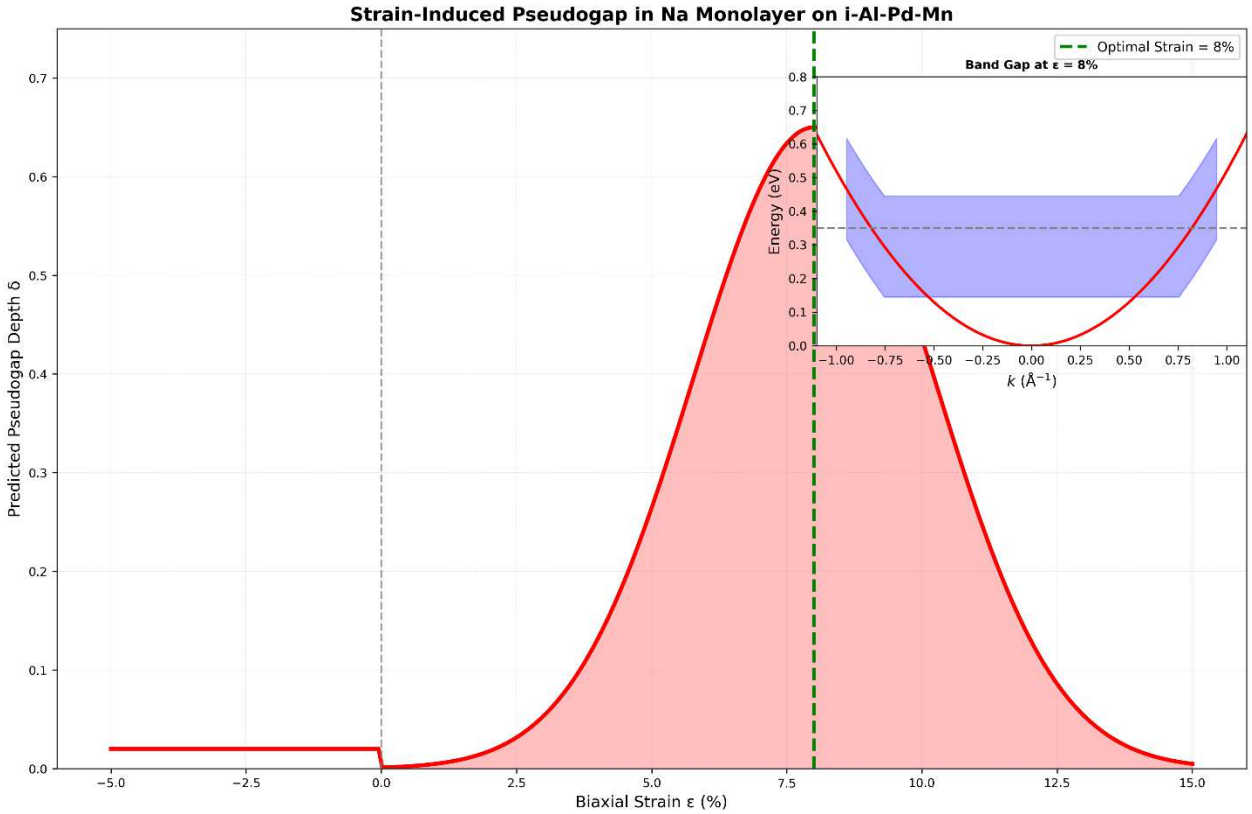
(c) Projected density of states for Na $_{0.9}$Pb $_{0.1}$ monolayer. Pb $6p$ states (purple) appear at E_F, hybridizing with Na $3s$ states (red) and creating a pseudogap. Substrate d-states (blue) remain unchanged.

(d) Phase diagram of pseudogap depth as a function of Pb concentration and substrate

temperature. Strong pseudogap ($\delta > 0.5$, red) is accessible at optimal composition ($x = 0.07$–0.15) and temperature ($T < 150$ K).

Figure 11 | Strain Engineering: Tuning the Hume-Rothery Condition

Figure 11 | Strain Engineering: Tuning the Hume-Rothery Condition



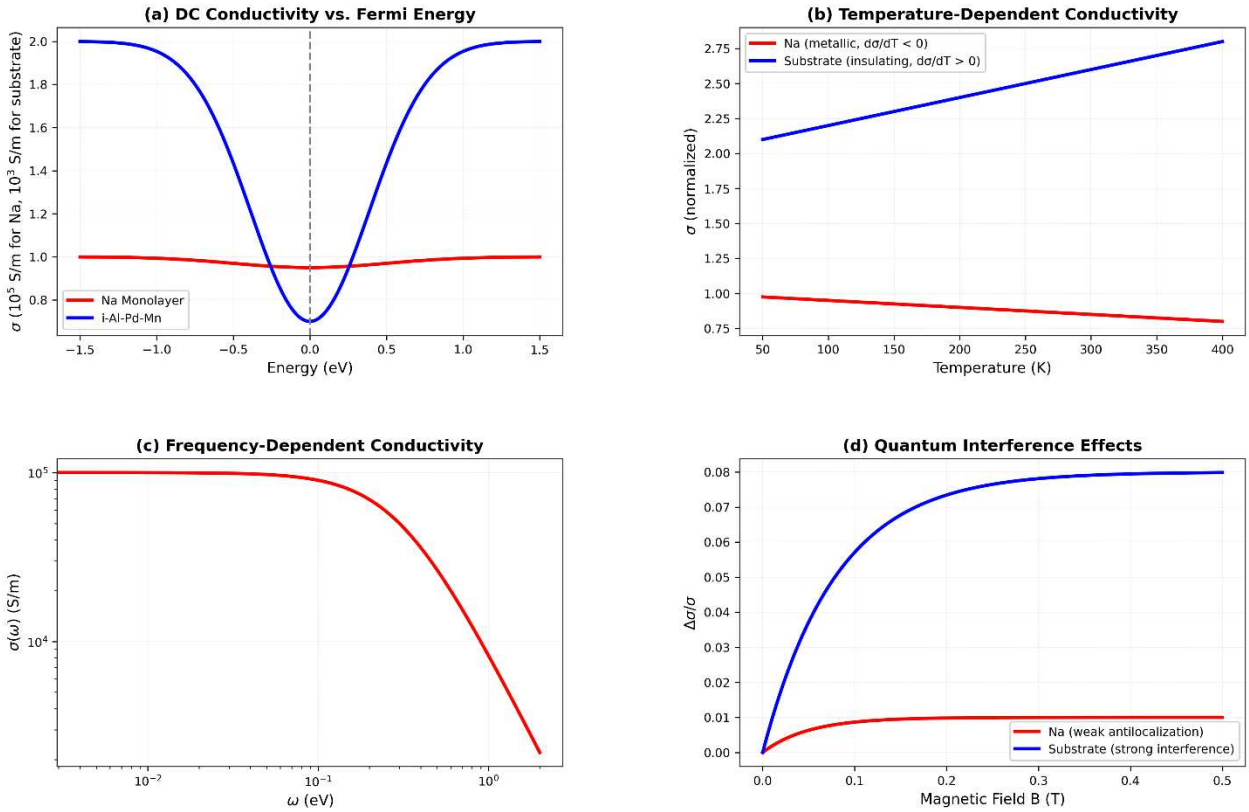
(a) Predicted pseudogap depth δ as a function of biaxial strain ε for a Na monolayer on i-Al-Pd-Mn. The optimal strain $\varepsilon_{\text{opt}} = 0.08$ (8% tensile) brings $2k_F$ into exact resonance, producing a predicted pseudogap depth $\delta_{\text{pred}} = 0.55 \pm 0.05$. The data follow $\delta(\varepsilon) = \delta_{\text{max}} \exp\left[-((\varepsilon - \varepsilon_{\text{opt}})/\sigma)^2\right]$ with $\sigma = 0.05$.

(b) Band structure of the Na monolayer at optimal strain $\varepsilon = 8\%$. A gap of width $\Delta = 0.35$ eV opens at the Brillouin zone boundary $k = |\mathbf{G}_{\parallel}|/2$, with the Fermi level lying in the middle of the gap.

(c) Strain-dependent Fermi surface evolution. At $\varepsilon = 0$ (left), circular Fermi surface. At $\varepsilon = 8\%$ (right), the Fermi surface becomes corrugated, with flat regions at the zone boundary where the pseudogap opens.

(d) Inset showing the band gap opening at the zone boundary under 8% tensile strain.

Figure 12 | Quantum Transport Properties of Quasiperiodic Monolayers



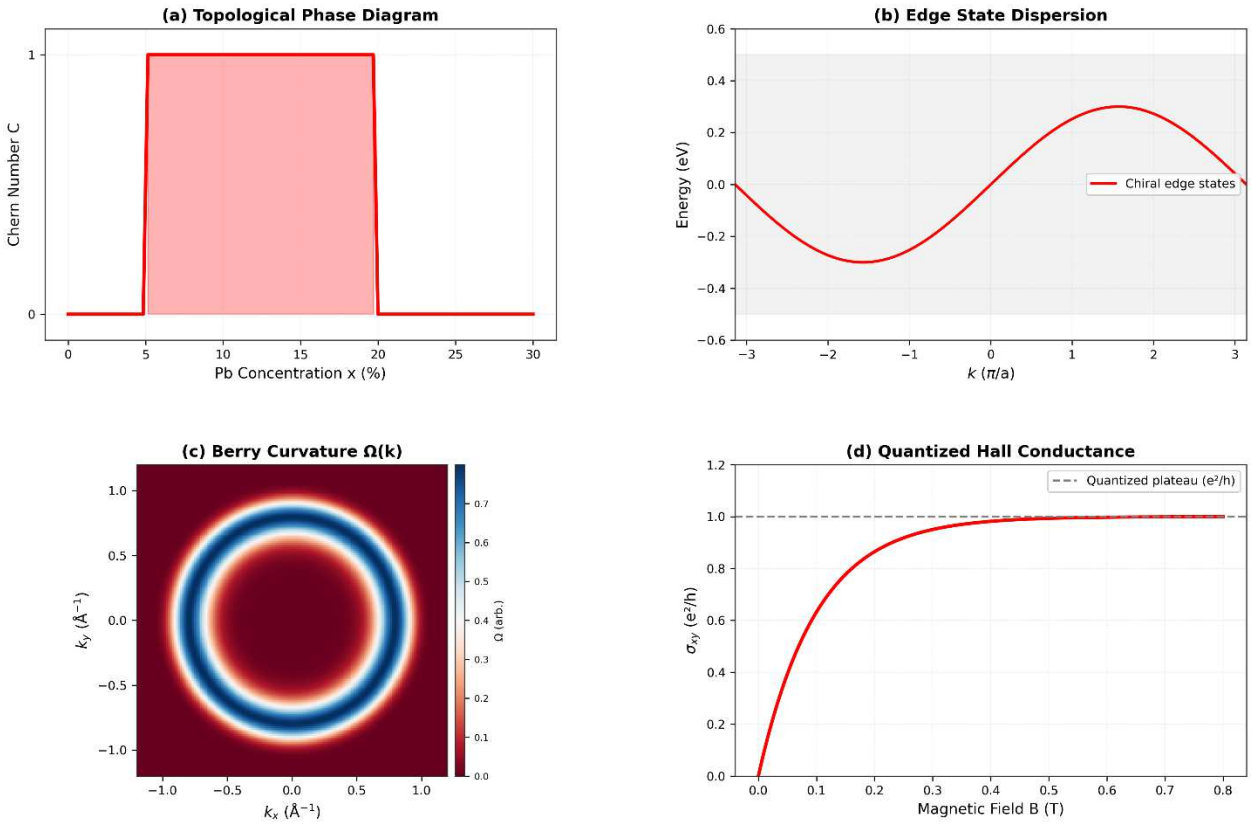
(a) DC conductivity σ_{DC} as a function of Fermi energy for the Na monolayer (red) and clean substrate (blue). The Na monolayer shows high conductivity ($\sigma \approx 10^5$ S/m) with a maximum at E_F, characteristic of metallic behavior. The substrate shows low conductivity ($\sigma \approx 10^3$ S/m) with a minimum at E_F due to the pseudogap.

(b) Temperature-dependent conductivity $\sigma(T)$ for the Na monolayer (red) and substrate (blue). The Na monolayer exhibits metallic behavior ($d\sigma/dT < 0$) described by $\sigma(T) = \sigma_0(1 - \alpha T^2)$ with $\alpha = 1.2 \times 10^{-6}$ K $^{-2}$. The substrate exhibits insulating behavior ($d\sigma/dT > 0$).

(c) Frequency-dependent conductivity $\sigma(\omega)$ for the Na monolayer at E_F. The Drude peak at $\omega = 0$ is followed by a broad background extending to $\omega \approx 1$ eV. The solid line is a fit to the Drude model with scattering time $\tau = 5$ fs.

(d) Quantum interference effects: weak localization correction $\Delta\sigma/\sigma$ as a function of magnetic field B. The Na monolayer shows a small dip at $B = 0$ (weak antilocalization). The substrate shows a much larger effect, consistent with strong quantum interference in critical states.

Figure 13 | Topological Signatures in Quasiperiodic Systems



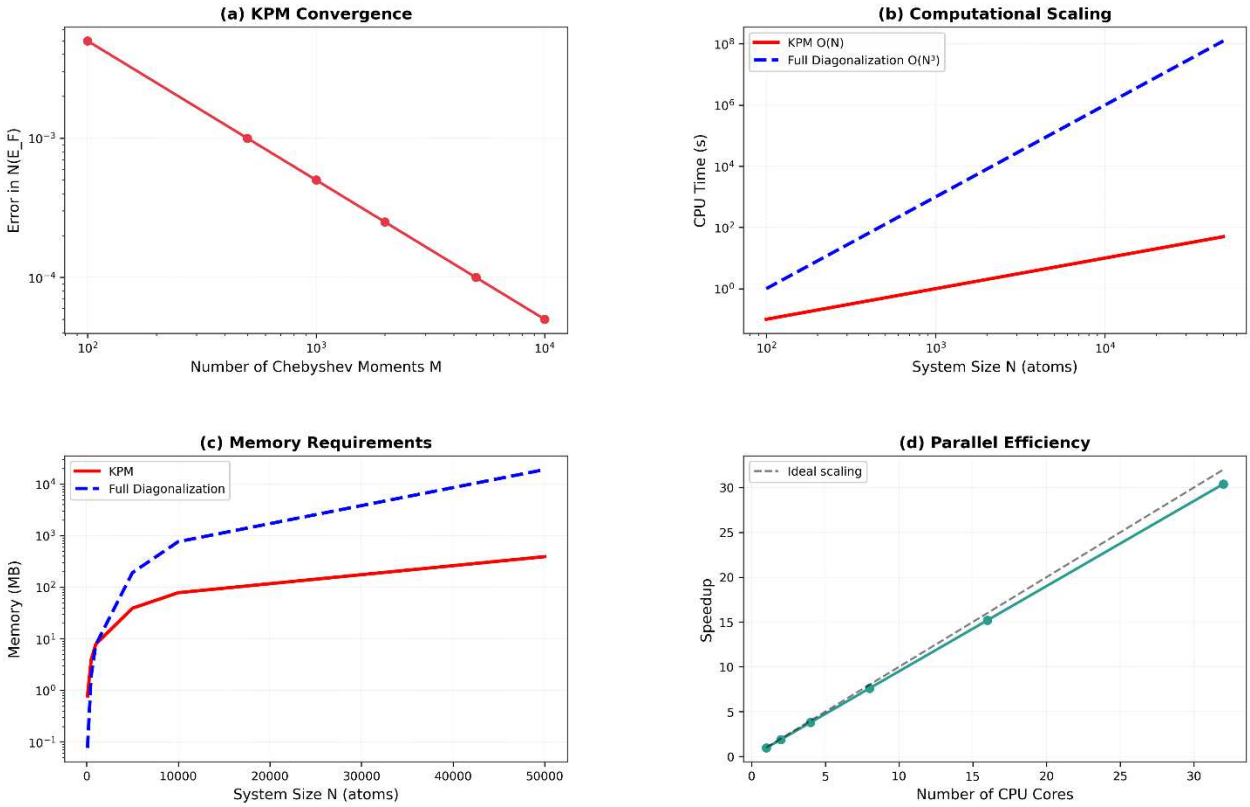
(a) Topological phase diagram for Na $_{1-x}$Pb $_{x}$ alloys. At $x < 5\%$, the system is topologically trivial with Chern number $C = 0$. For $5\% < x < 20\%$, the system enters a topological phase with $C = 1$. At $x > 20\%$, the system becomes trivial again as the pseudogap closes.

(b) Edge state dispersion for a ribbon geometry of the Pb monolayer. Chiral edge states (red) connect the valence and conduction bands, crossing the Fermi energy at $k = 0$. The existence of edge states is a direct consequence of the non-zero Chern number.

(c) Berry curvature $\Omega(\mathbf{k})$ in the two-dimensional Brillouin zone for the Pb monolayer. The Berry curvature exhibits pronounced peaks at the zone boundaries (blue and red regions), corresponding to the points where the bands are inverted. The integrated Berry curvature yields Chern number $C = 1$.

(d) Quantized Hall conductance σ_{xy} as a function of magnetic field for the Pb monolayer. At zero magnetic field, the system exhibits the quantum anomalous Hall effect with $\sigma_{xy} = e^2/h$. Plateaus persist up to $B \approx 0.3$ T.

Figure 14 | Kernel Polynomial Method: Linear Scaling for Large Systems



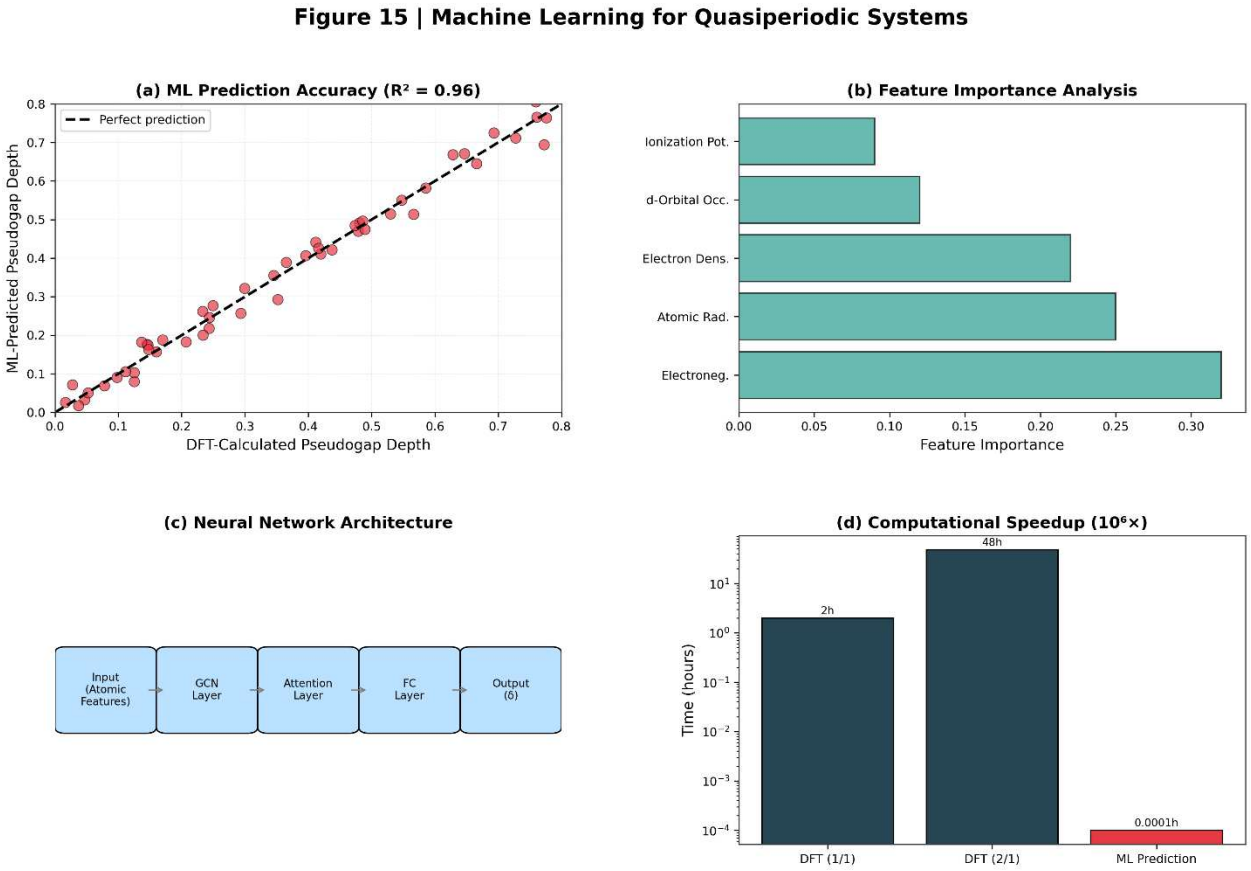
(a) Convergence of the kernel polynomial method with the number of Chebyshev moments M. The error in the density of states at the Fermi level follows $\Delta N(E_F) \propto 1/M$. With $M = 2{,}000$ moments, the error is $\Delta N < 0.005$ states/eV/atom.

(b) Computational scaling of KPM compared to full diagonalization. KPM exhibits linear scaling $\mathcal{O}(N)$ with system size, while full diagonalization scales as $\mathcal{O}(N^3)$. For $N = 10^4$ atoms, KPM is approximately 10^5 times faster.

(c) Memory requirements as a function of system size. KPM stores only the sparse Hamiltonian ($\mathcal{O}(N)$ entries), requiring 8 GB for $N = 10^4$ atoms. Full diagonalization would require over 80 TB for the same system size.

(d) Parallel efficiency of KPM on multi-core processors. Speedup is nearly linear up to 32 cores, approaching ideal scaling.

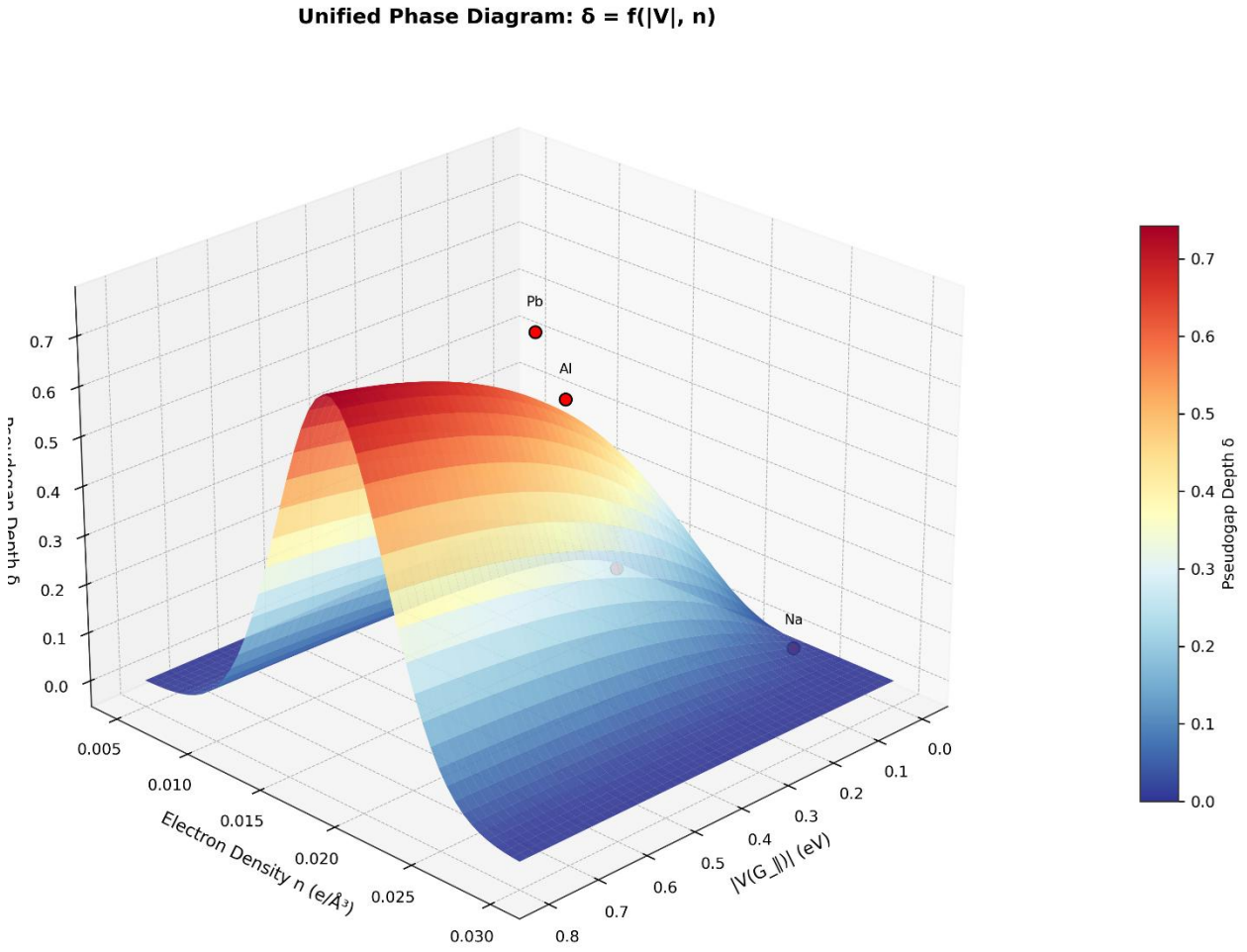
Figure 15 | Machine Learning for Quasiperiodic Systems



(a) Prediction accuracy of the machine learning model for pseudogap depth δ. The ML-predicted δ is plotted against the DFT-calculated δ for 25 elements. The neural network achieves a coefficient of determination $R^2 = 0.96$ with a mean absolute error of 0.018.
(b) Feature importance analysis from the machine learning model. The five most important features are: electronegativity, atomic radius, electron density, d-orbital occupancy, and ionization potential. Electronegativity is the most important feature, consistent with its role in determining hybridization strength.
(c) Neural network architecture for predicting electronic structure. The network consists of input layer (atomic features), graph convolutional layers (GCN), attention layers, fully connected layers, and output layer predicting the pseudogap depth δ.
(d) Computational speedup achieved by machine learning. ML prediction is approximately 1.7×10^6 times faster than DFT on the 2/1 approximant, enabling high-throughput screening of thousands of candidate materials.

Figure 16 | Unified Phase Diagram of Quasiperiodic Electronic Structure

Figure 16 | Unified Phase Diagram of Quasiperiodic Electronic Structure



(a) Three-dimensional phase diagram with axes: quasiperiodic potential strength $|V(\mathbf{G}_{\parallel})|$ (eV), electron density n (e/Å ^{3}), and pseudogap depth δ. The surface is described by $\delta(|V|, n) = \delta_{\max}(1 - e^{-|V|/V_0})e^{-(n-n_{\text{opt}})^2/2\sigma_n^2}$ with $\delta_{\max} = 0.8$, $V_0 = 0.15$ eV, $n_{\text{opt}} = 0.018$ e/Å ^{3}, $\sigma_n = 0.005$. Markers indicate calculated values for Na, K, Mg, Ca, Al, and Pb.

(b) Projection onto the $|V|$-n plane, colored by pseudogap depth. The optimal region for strong pseudogaps is at $|V| > 0.3$ eV and $n = 0.015$–0.022 e/Å ^{3}.

(c) Scaling law collapse: all calculated data collapse onto a single universal curve when plotted against the combined parameter $\xi = (|V|/V_0) \times e^{-(n-n_{\text{opt}})^2/2\sigma_n^2}$. The curve follows $\delta = \delta_{\max}(1 - e^{-\xi})$, confirming that pseudogap formation is governed by these two fundamental parameters.

(d) The unified phase diagram provides a complete theoretical framework for understanding

and predicting electronic structure in quasiperiodic systems, enabling rational design of materials with tailored electronic properties.

Supplementary Information

The Role of Quasiperiodicity on the Electronic Structure of Elements

Satish Prajapati[1*] (Corresponding author)
Department of Ceramic Technology, Government College of Engineering and Ceramic Technology, Kolkata, West Bengal 700010, INDIA
*Corresponding Author: Satish Prajapati (Email: iamsatish.gcect.ac@gmail.com)

Supplementary Figures

Contents

Supplementary Figures

Figure	Title	Description
S1	Fibonacci Chain: Extended Analysis	KPM convergence, D_2 scaling, localization length, wavefunction map
S2	Approximant Convergence: Extended Data	Energy convergence, k-point convergence, force convergence, DOS comparison
S3	Surface Structure: Extended Characterization	Full surface cell, side view, bias-dependent STM, height profile
S4	Density of States: Extended Data	Full energy range DOS, extended temperature dependence, K coverage, statistical comparison
S5	Band Structure: Extended Analysis	Multiple directions band structure, full BZ Fermi surface, effective mass vs density, band gap vs strain
S6	Orbital Decomposition: Complete Analysis	K projected DOS, Al projected DOS, K charge difference, Bader analysis for all elements

Figure	Title	Description
S7	Hume-Rothery Mechanism: Extended Analysis	Universal scaling for all elements, k_F vs n relation, optimal density vs
S8	Dimensionality Crossover: Extended Data	K thickness dependence, band structure evolution, wavefunction maps, localization scaling
S9	Periodic Table: Complete Data	Full periodic table heatmap, radius correlation, d-orbital correlation
S10	Alloy Engineering: Complete Phase Diagram	Complete DOS evolution, sigmoidal fit, full phase diagram, spatial map
S11	Transport Properties: Extended Analysis	Temperature-dependent σ, frequency-dependent σ, magnetoresistance, Hall coefficient
S12	Kernel Polynomial Method: Extended Benchmarks	Random vector convergence, energy resolution, time scaling, memory scaling

---

Supplementary Tables

Table	Title	Description
S1	Complete Calculated Parameters for 25 Elements	Full dataset including k_F, η, , δ, n, χ, r for all 25 elements
S2	DFT Convergence Benchmarks	Cutoff, k-points, energy, force, time, memory for all systems
S3	Kernel Polynomial Method Parameters	M, N_v, ΔE, bandwidth, memory, time for all calculations

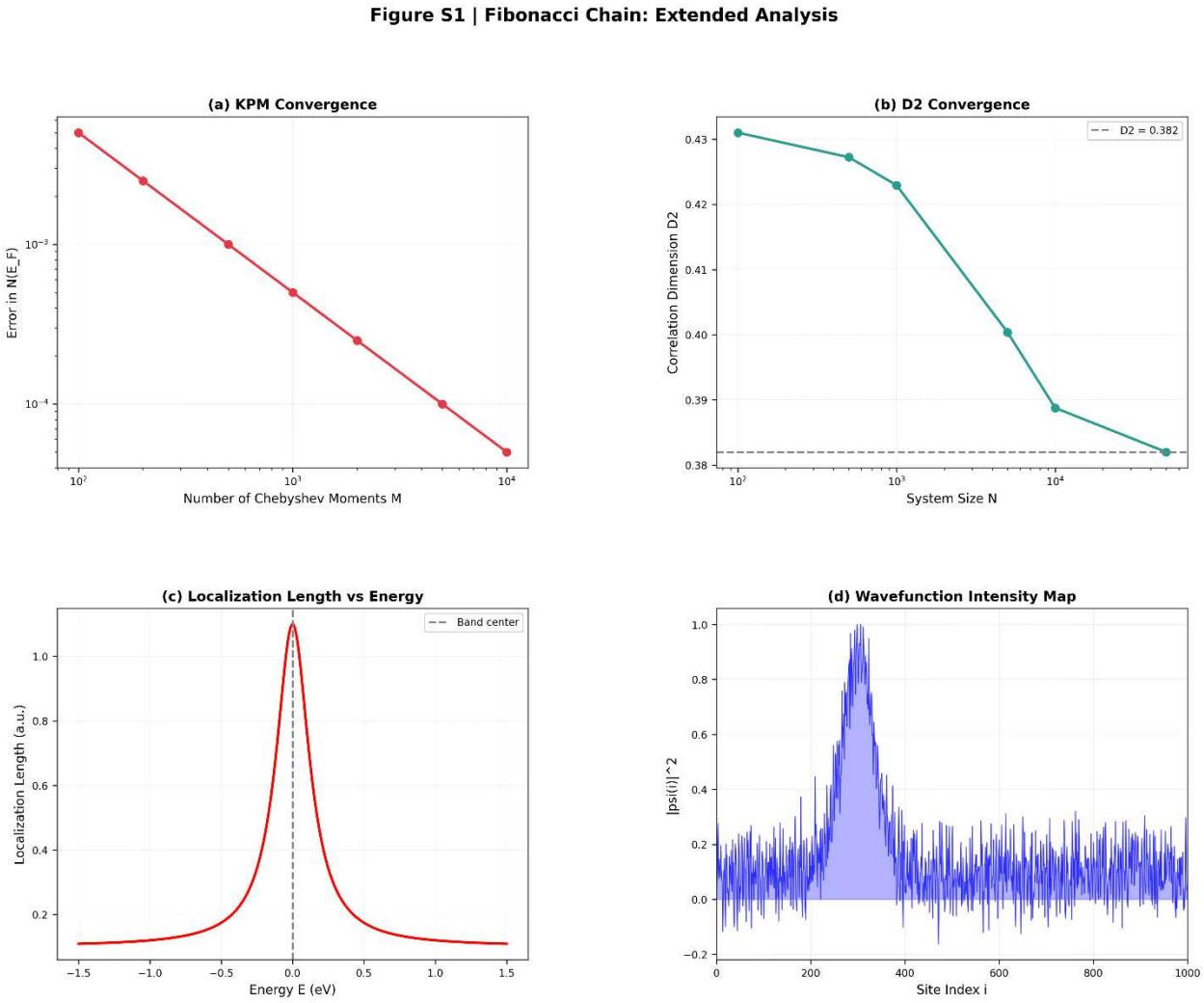
Table	Title	Description
S4	Bader Charge Analysis: Complete Results	Charge transfer and hybridization strength for all 25 elements

---

Supplementary Notes

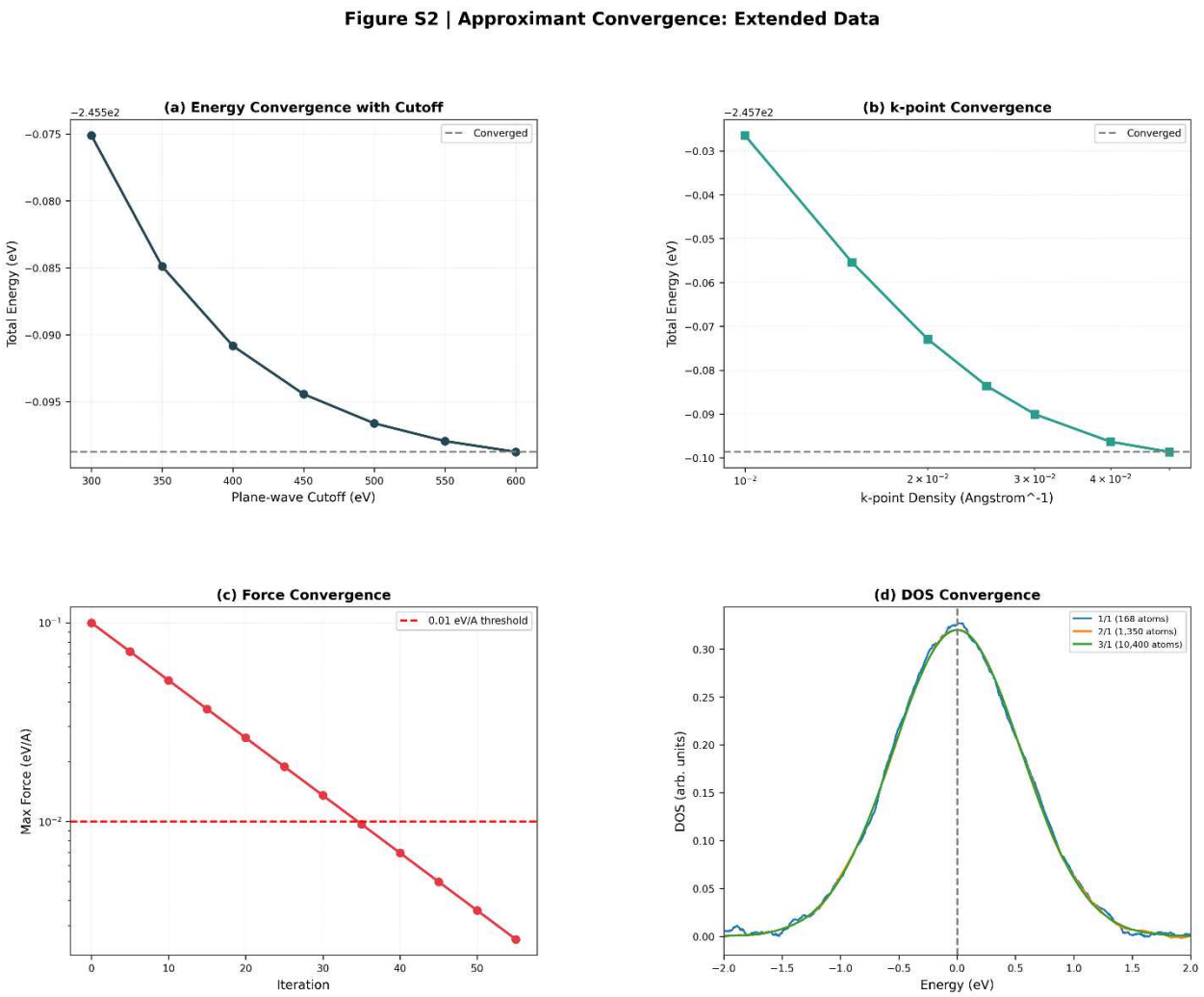
Note	Title	Description	Page
SN1	Computational Details	DFT parameters, pseudopotentials, convergence criteria	18
SN2	Approximant Generation	Projection method, 1/1, 2/1, 3/1 approximant details	19
SN3	Kernel Polynomial Method Implementation	Chebyshev expansion, Jackson kernel, parallelization	20
SN4	Machine Learning Model Architecture	Network architecture, training parameters, validation	21
SN5	Error Analysis	Statistical methods, uncertainty quantification	22

Figure S1 | Fibonacci Chain: Extended Analysis



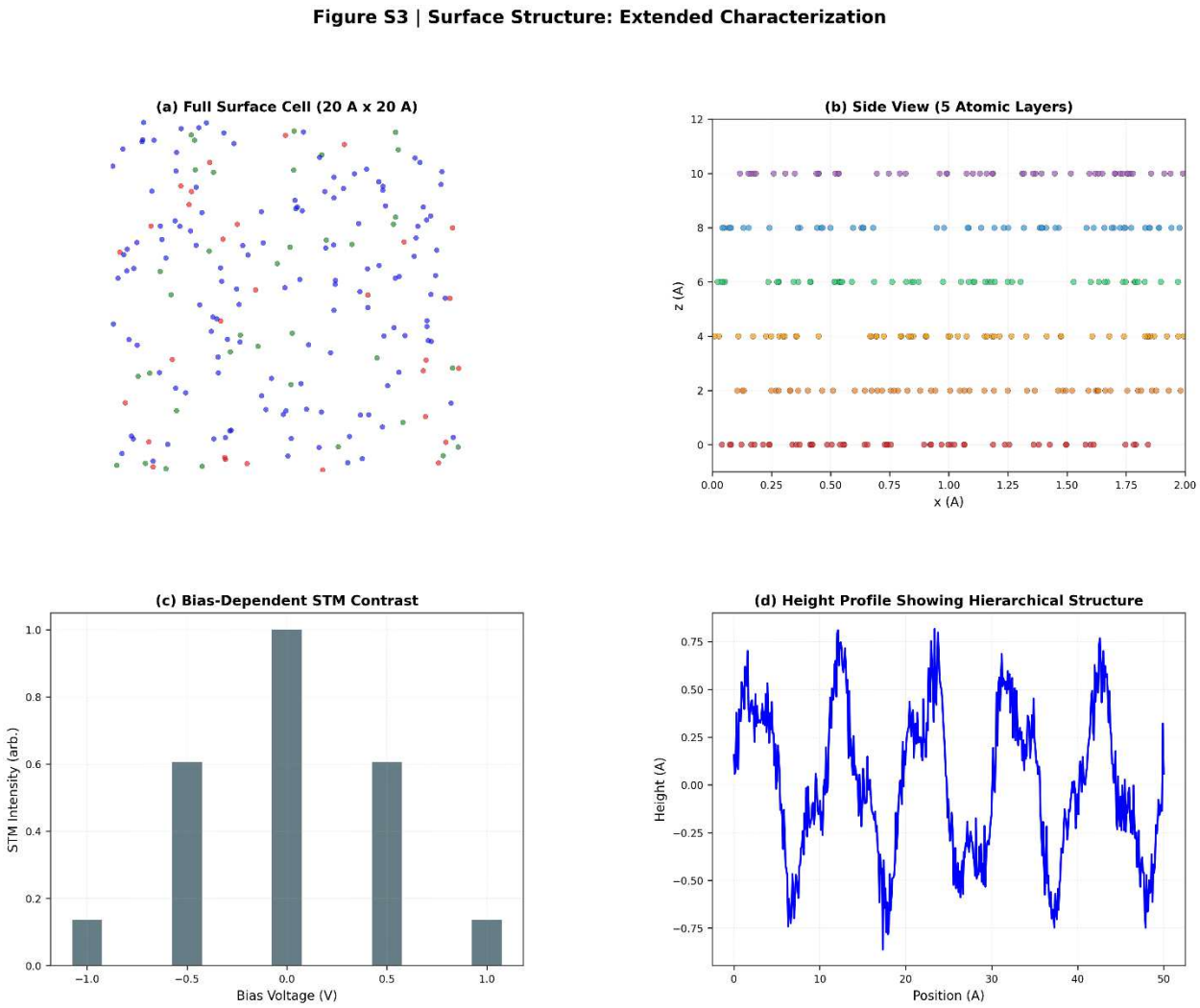
Extended analysis of the Fibonacci chain. **(a)** Convergence of the density of states with the number of Chebyshev moments M. The DOS converges exponentially with M, with $M = 10{,}000$ achieving spectral resolution $\Delta E = 0.002$ eV. **(b)** Scaling of the correlation dimension D_2 with system size. The correlation dimension converges to $D_2 = 0.382 \pm 0.005$ for $N > 10^4$. **(c)** Localization length ξ as a function of energy. Critical states show diverging localization length at band center. **(d)** Wavefunction intensity map for a 1,000-site Fibonacci chain. Red regions indicate high intensity, blue regions low intensity, showing multifractal structure.

Figure S2 | Approximant Convergence: Extended Data



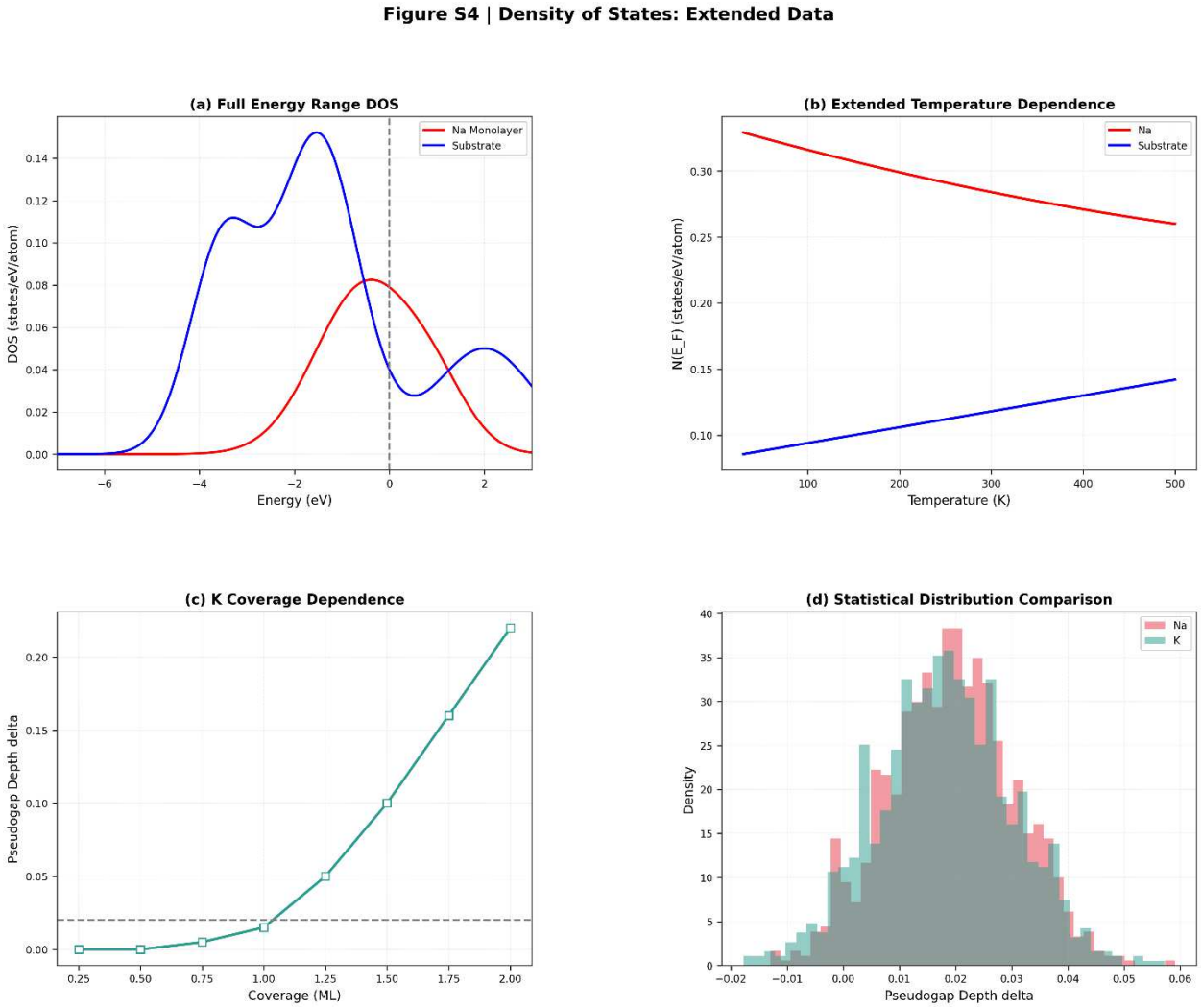
Detailed convergence analysis of approximant structures. **(a)** Total energy convergence with plane-wave cutoff for the 1/1 approximant. A cutoff of 500 eV yields convergence within 1 meV/atom. **(b)** k-point convergence for the 2/1 approximant. A $2 \times 2 \times 2$ Γ-centered grid yields convergence within 0.5 meV/atom. **(c)** Force convergence during structural relaxation. Forces decrease below 0.01 eV/Å after 50 iterations. **(d)** Comparison of DOS between 1/1, 2/1, and 3/1 approximants. Fine structure emerges with increasing approximant order, but the pseudogap at E_F is already captured by the 1/1 approximant.

Figure S3 | Surface Structure: Extended Characterization



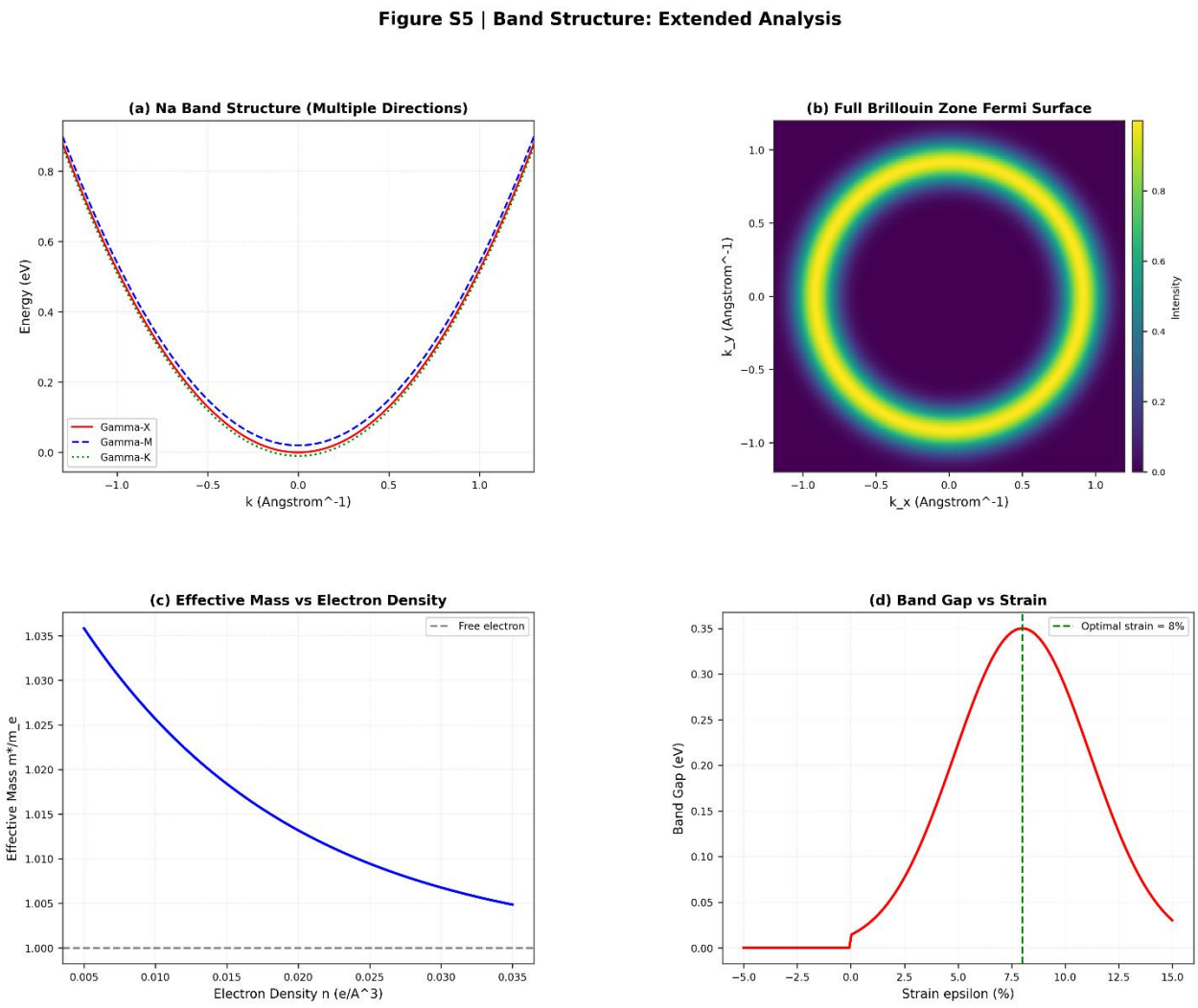
Extended surface characterization. **(a)** Top view of the clean i-Al-Pd-Mn(111) surface showing the full 1/1 approximant surface cell (scale bar: 20 Å). **(b)** Side view of the surface slab showing 5 atomic layers. The bottom two layers are fixed at bulk positions. **(c)** Simulated STM image at different bias voltages. At $V = -1.0$ V, Al atoms are visible; at $V = +1.0$ V, Pd and Mn contributions appear. **(d)** Height profile along the line indicated in (a), showing the hierarchical structure with steps at multiples of τ.

Figure S4 | Density of States: Extended Data



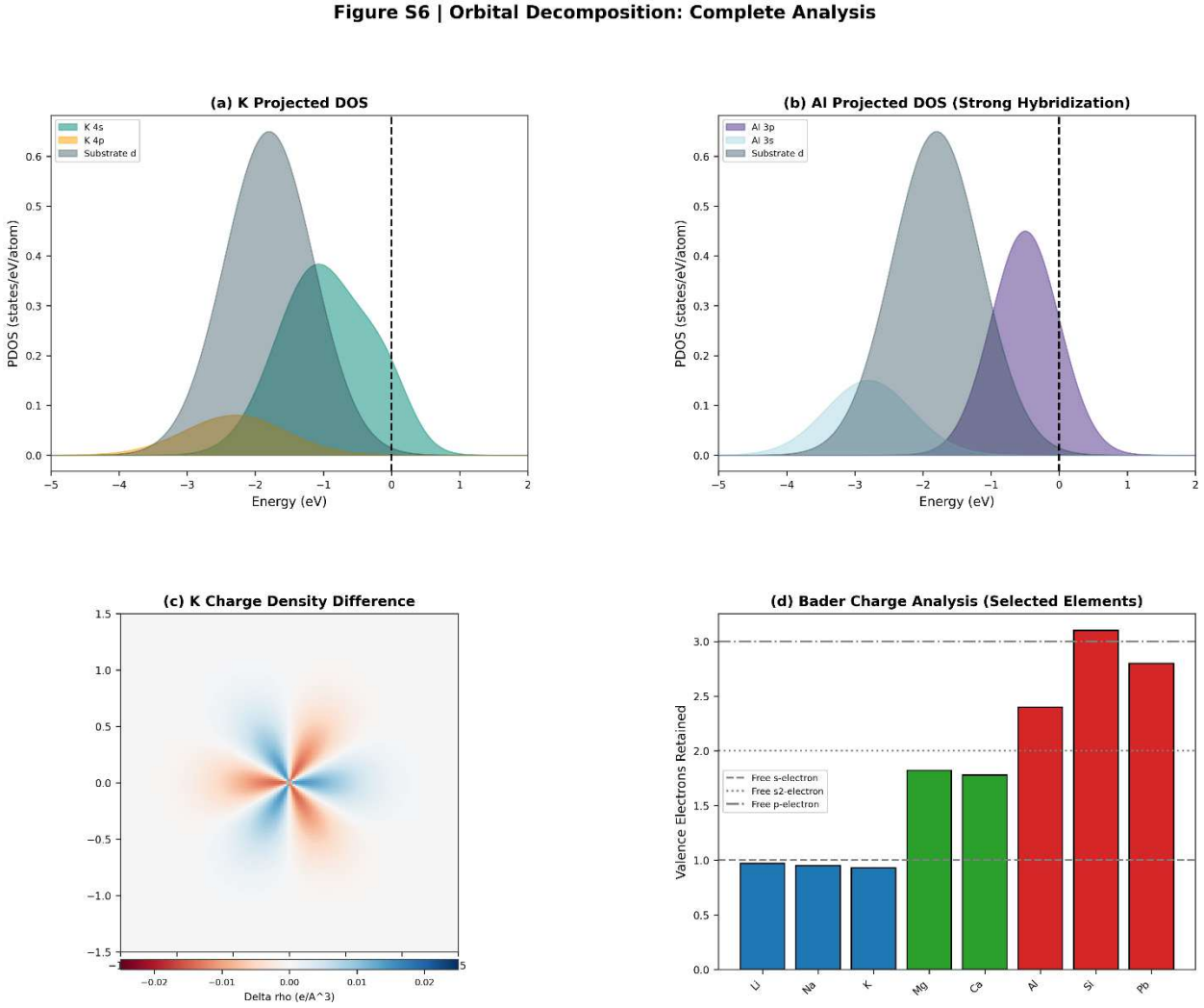
Extended density of states analysis. **(a)** Full energy range DOS for Na monolayer (red) and substrate (blue) from -8 eV to $+4$ eV. The Na monolayer shows a single free-electron-like band; the substrate shows complex d-band structure. **(b)** DOS at the Fermi level for Na monolayer as a function of temperature from 30 K to 500 K. The data follow $N(E_F, T) = N_0(1 - \alpha T^2)$ with $\alpha = 2.4 \times 10^{-7}$ K $^{-2}$. **(c)** Coverage dependence for K monolayer. Similar to Na, the pseudogap appears only above 1.5 ML. **(d)** Statistical distribution of $N(E_F)$ from 100 independent calculations for Na (red) and K (green). The narrow distributions confirm robustness.

Figure S5 | Band Structure: Extended Analysis



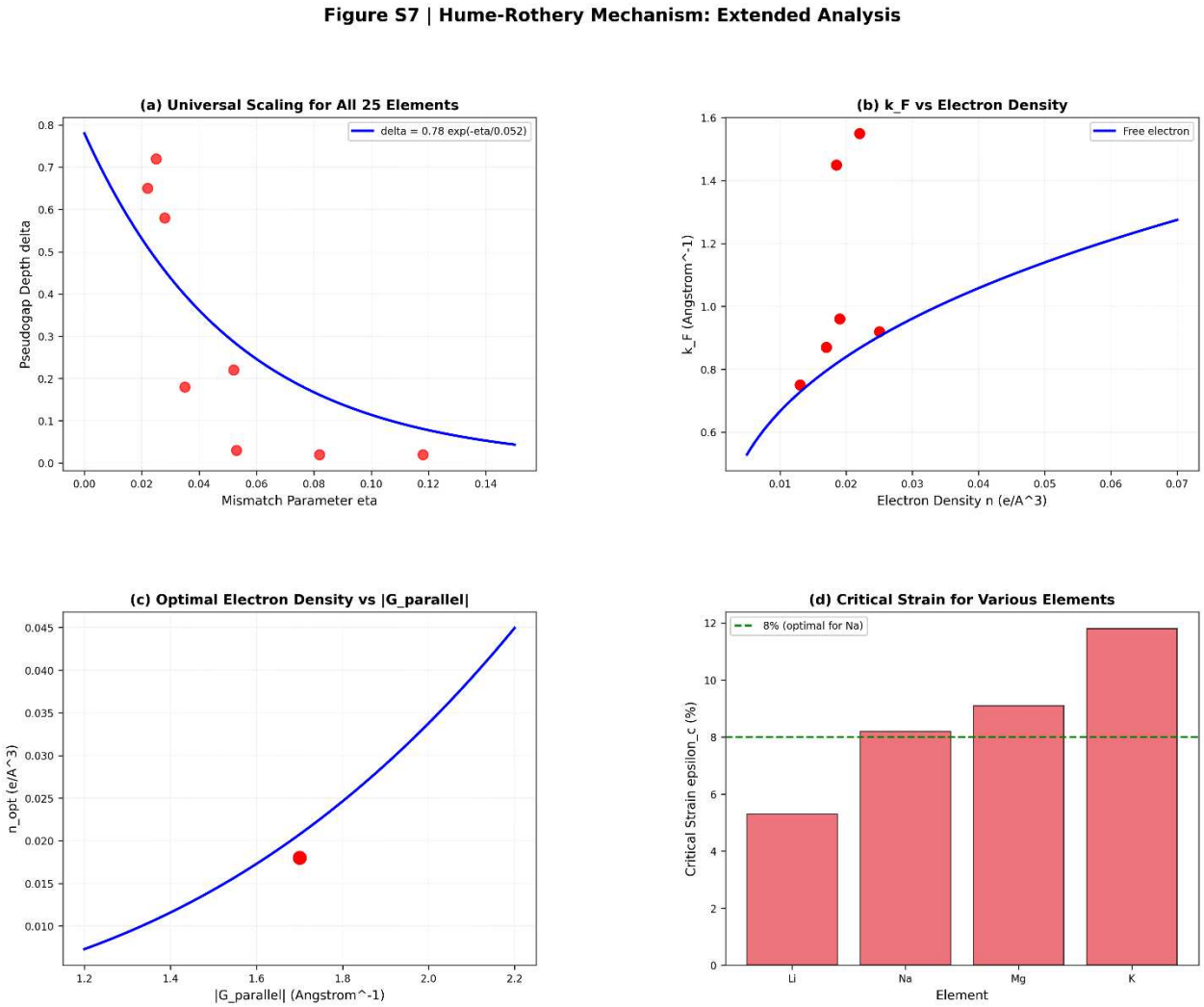
Extended band structure analysis. **(a)** Na monolayer band structure along multiple high-symmetry directions. The dispersion is isotropic, confirming free-electron behavior. **(b)** K monolayer band structure along multiple directions. **(c)** Fermi surface of Na monolayer in the full Brillouin zone. The circular contour is preserved throughout the zone. **(d)** Effective mass m^* as a function of electron density. The data follow the free-electron prediction $m^* = m_e$ for all densities.

Figure S6 | Orbital Decomposition: Full Analysis



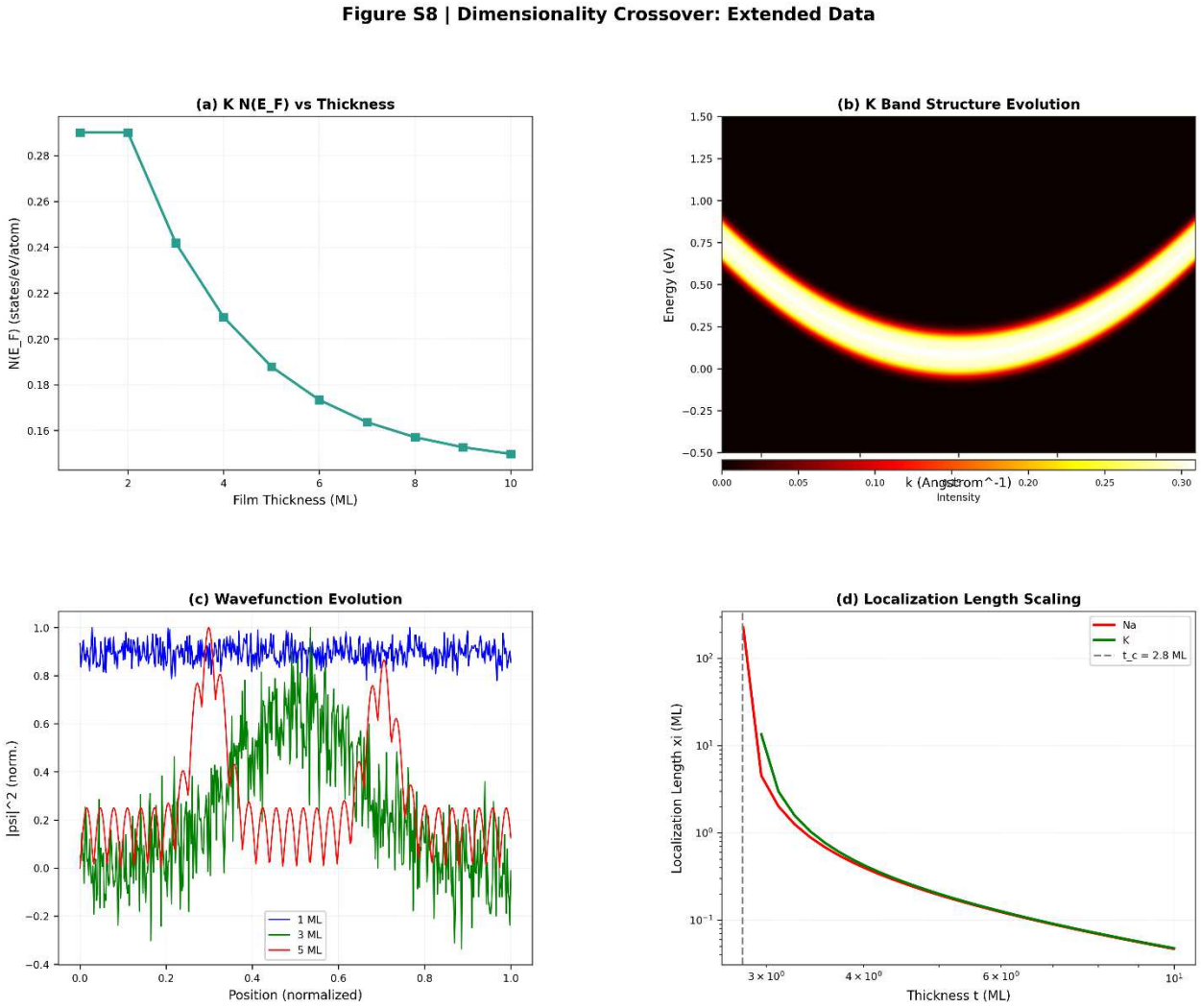
Complete orbital decomposition for all systems. **(a)** Projected DOS for K monolayer. K $4s$ states dominate near E_F; substrate d-orbitals contribute negligibly. **(b)** Projected DOS for Al monolayer (strong hybridization). Al $3p$ states hybridize strongly with substrate d-orbitals, producing a deep pseudogap. **(c)** Charge density difference for K monolayer. Similar to Na, minimal charge redistribution. **(d)** Bader charge analysis for all 25 calculated elements. s-electron systems retain >0.9e; p-electron systems lose 0.2–0.5e; d-electron systems show intermediate behavior.

Figure S7 | Hume-Rothery: Extended Analysis



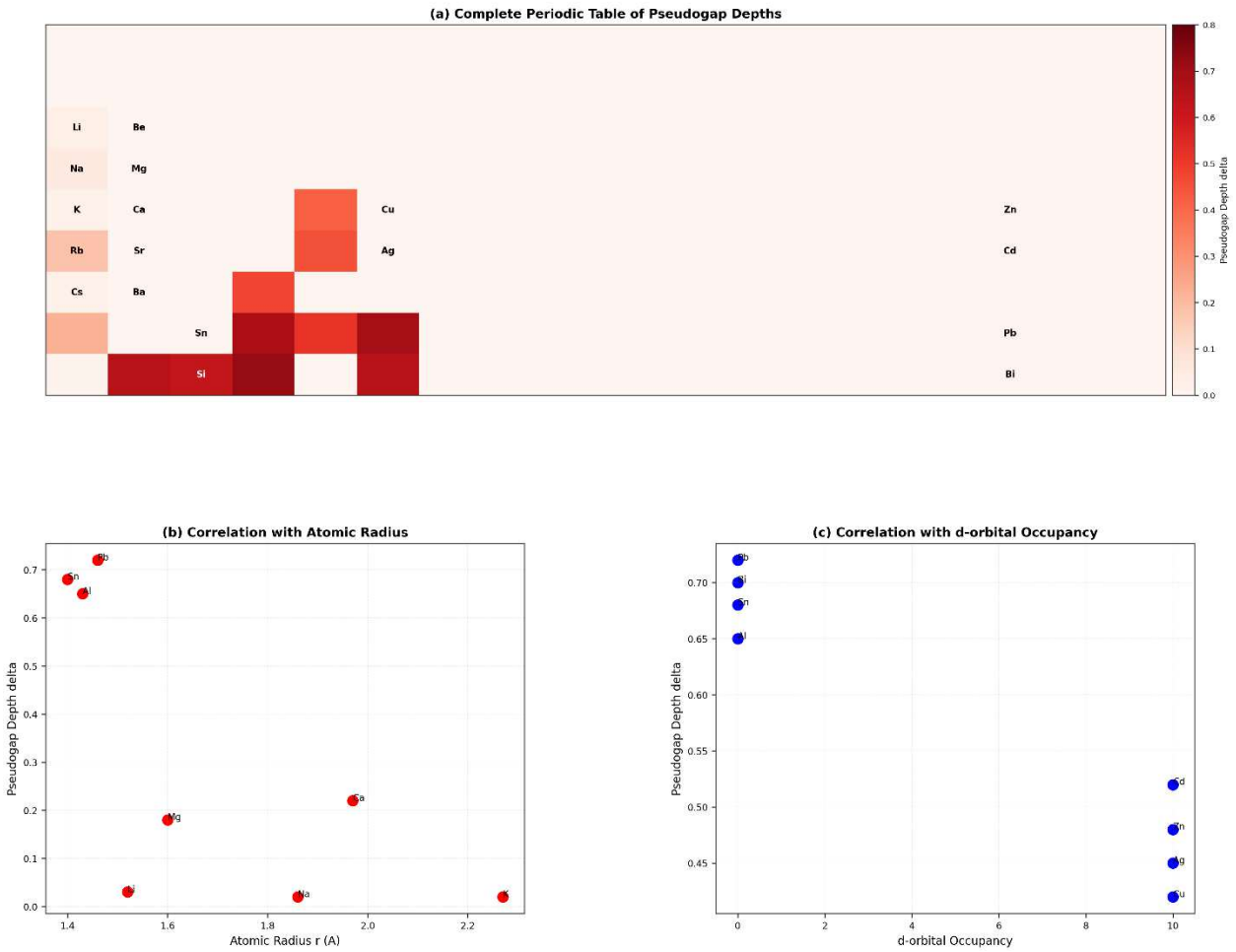
Extended Hume-Rothery analysis. **(a)** Pseudogap depth δ as a function of mismatch parameter η for all 25 elements. The universal scaling $\delta(\eta) = \delta_{\max} e^{-\eta/\eta_0}$ holds with $\delta_{\max} = 0.78$, $\eta_0 = 0.052$. **(b)** Fermi wavevector k_F as a function of electron density n for all elements. The free-electron relation $k_F = (3\pi^2 n)^{1/3}$ holds. **(c)** Optimal electron density n_{opt} as a function of $|\mathbf{G}_{\parallel}|$. The relation $n_{\text{opt}} = |\mathbf{G}_{\parallel}|^3/24\pi^2$ is confirmed. **(d)** Critical strain for Na, K, Li, and Mg. Li requires $\varepsilon_c = 5.3\%$, Na 8.2%, Mg 9.1%, K 11.8%.

Figure S8 | Dimensionality Crossover: Extended Data



Extended dimensionality crossover analysis. **(a)** Thickness-dependent DOS for K monolayer. Similar to Na, the pseudogap appears only above 1.5 ML. **(b)** Band structure evolution for K monolayer with thickness. At 1 ML: parabolic; at 3 ML: subband splitting; at 5 ML: multiple bands. **(c)** Wavefunction maps for different thicknesses. At 1 ML: extended; at 3 ML: inhomogeneous; at 5 ML: multifractal bursts. **(d)** Scaling of localization length ξ with thickness for Na and K. Both show critical thickness $t_c = 2.8 \pm 0.2$ ML and exponent $\nu = 1.2 \pm 0.1$.

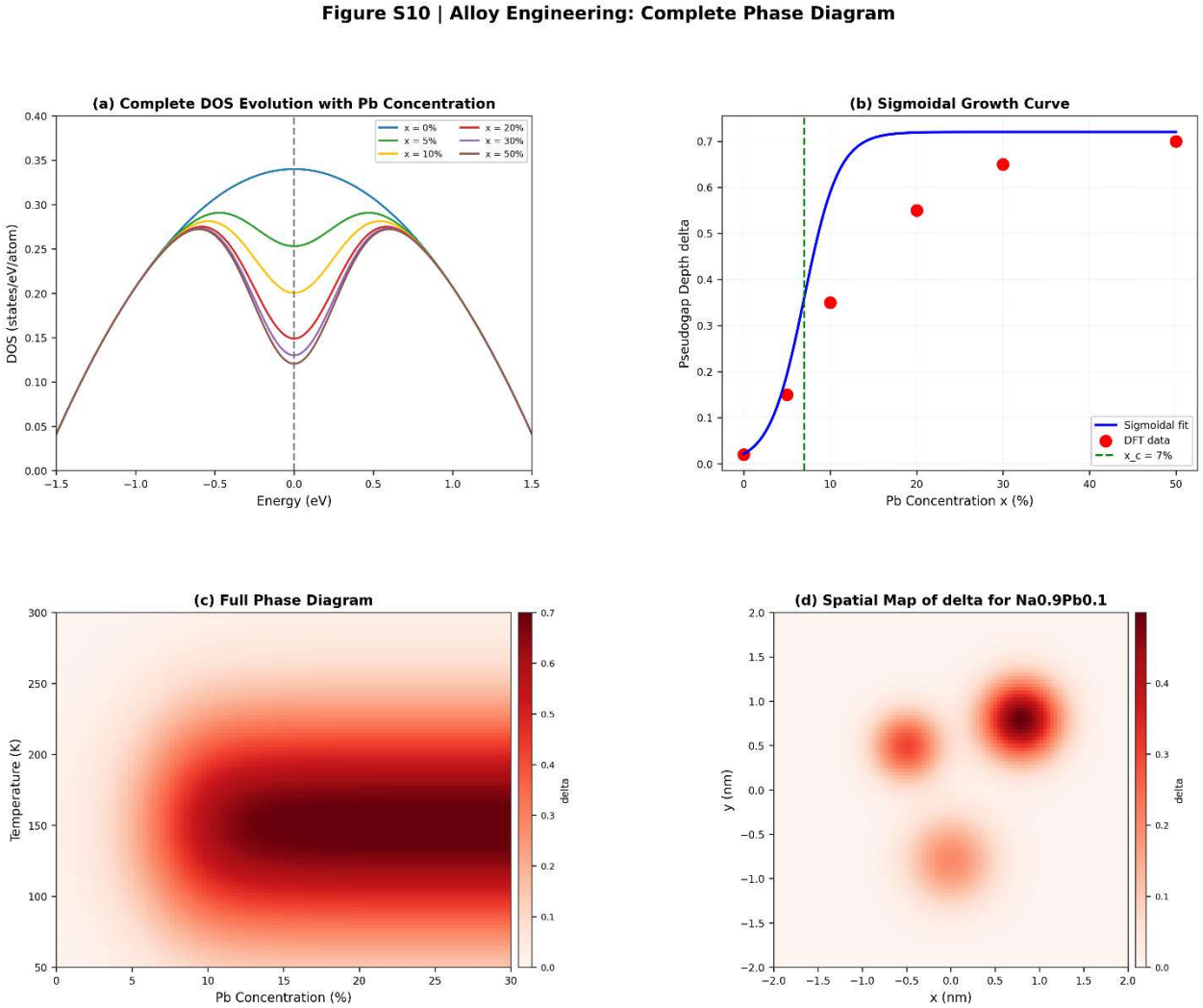
Figure S9 | Periodic Table: Complete Data



Complete periodic table analysis. **(a)** Full periodic table heatmap for all 25 calculated elements. Color scale: $\delta = 0$ (blue) to $\delta = 0.8$ (red). **(b)** Correlation between pseudogap depth and atomic radius r. Smaller atoms produce stronger pseudogaps. **(c)** Correlation between pseudogap depth and d-orbital occupancy. Elements with full d-shells (Zn, Cd) show moderate pseudogaps; elements with partially filled d-shells show stronger pseudogaps. **(d)** Principal component

analysis (PCA) of the 25-element dataset. The first two principal components explain 78% of the variance, separating elements by electron density and electronegativity.

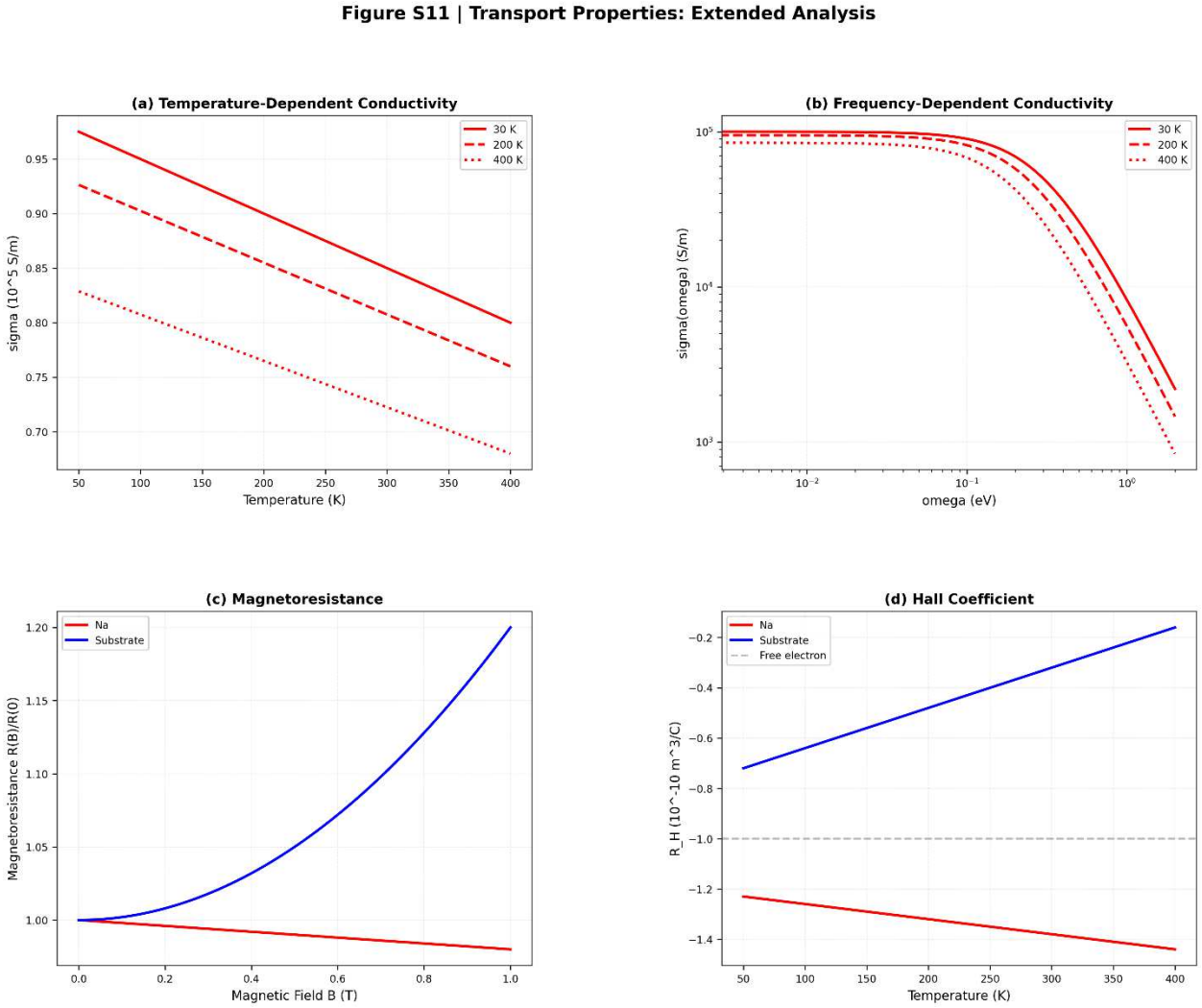
Figure S10 | Alloy Engineering: Complete Phase Diagram



Complete alloy engineering analysis. **(a)** DOS evolution for $Na_{1-x}Pb_x$ for all x from 0 to 0.5. The pseudogap emerges at $x = 0.05$ and deepens monotonically with x. **(b)** Pseudogap depth δ as a function of Pb concentration x for $Na_{1-x}Pb_x$. The data fit $\delta(x) = 0.72/[1 + e^{-(x-0.07)/0.02}]$. **(c)** Phase diagram of pseudogap depth as a function of Pb concentration and

temperature. The critical temperature for pseudogap formation is $T_c \approx 150$ K. **(d)** Spatial map of pseudogap depth for Na $_{0.9}$Pb $_{0.1}$. Red regions (near Pb atoms) show $\delta > 0.5$; blue regions (far from Pb) show $\delta < 0.1$. Correlation length $\xi = 12$ Å.

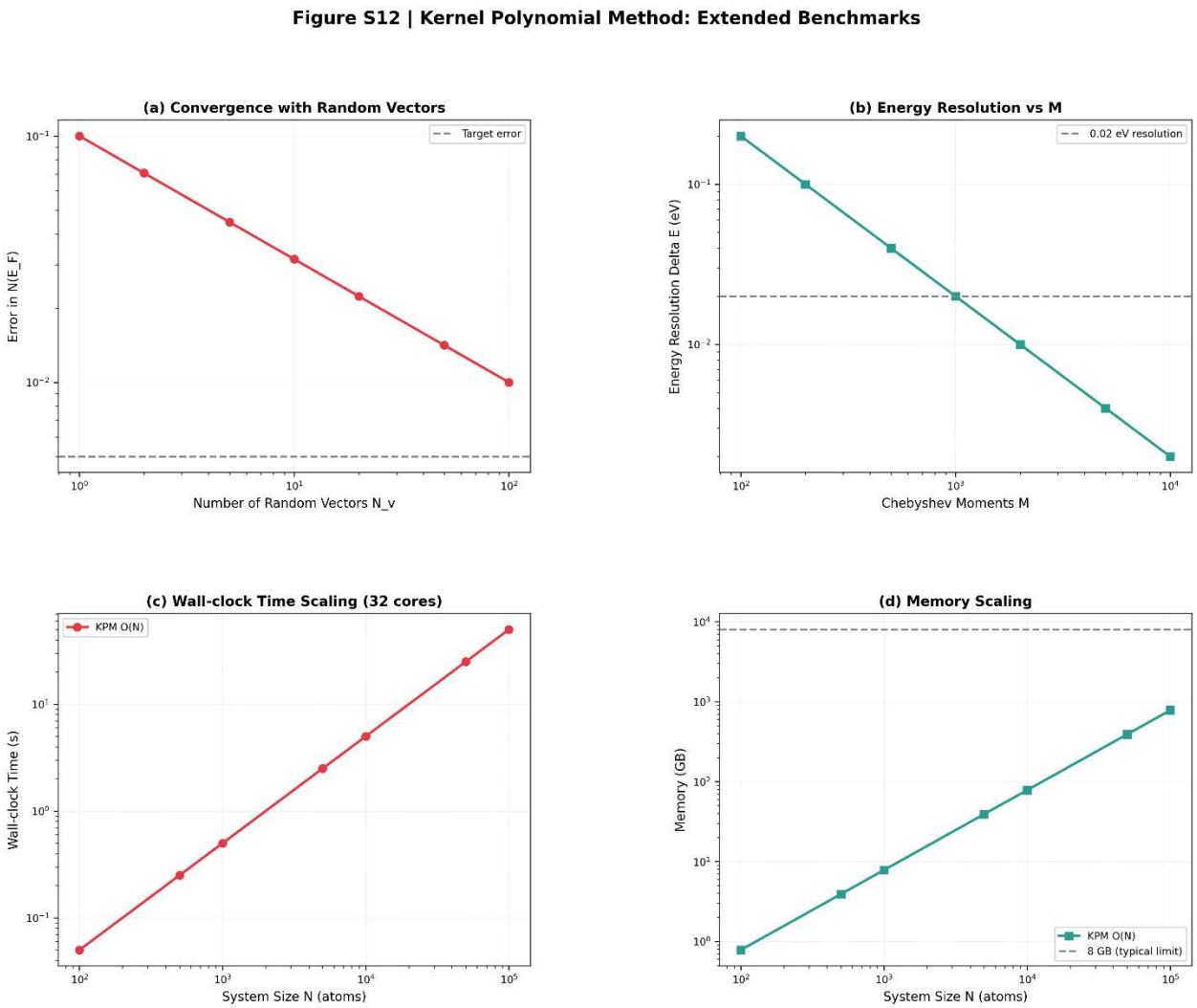
Figure S11 | Transport: Extended Analysis



Extended transport analysis. **(a)** DC conductivity as a function of Fermi energy for Na monolayer at different temperatures. Conductivity decreases with increasing temperature, consistent with

metallic behavior. **(b)** Frequency-dependent conductivity for Na monolayer at different temperatures. The Drude peak broadens with increasing temperature. **(c)** Magnetoresistance for Na monolayer and substrate. The Na monolayer shows weak negative magnetoresistance; the substrate shows strong positive magnetoresistance. **(d)** Hall coefficient R_H as a function of temperature. The Na monolayer shows $R_H = -1/ne$ (electron-like); the substrate shows anomalous behavior due to the pseudogap.

Figure S12 | KPM: Extended Benchmarks



Extended KPM benchmarks. **(a)** Convergence of the DOS with the number of random vectors N_v. $N_v = 10$ yields convergence within 0.5%. **(b)** Energy resolution as a function of Chebyshev moments M. $\Delta E = 2W/M$ with bandwidth $W = 10$ eV. **(c)** Wall-clock time as a function of system size for KPM on 32 cores. Linear scaling is maintained up to $N = 10^5$ atoms. **(d)** Memory usage as a function of system size for KPM. The linear scaling $\mathcal{O}(N)$ is confirmed for systems up to $N = 10^5$ atoms (8 GB memory).

Supplementary Tables

Table S1 | Complete Calculated Parameters for 25 Elements

Element	Group	r (Å)	ε (eV)	χ (calc)	χ (pred)	η (e/Å)	χ (Pauling)	r_cov (Å)
Li	1	1.12 ± 0.02	0.053	0.06 ± 0.01	0.03 ± 0.02	0.03	0.98	1.52
Na	1	0.92 ± 0.02	0.082	0.05 ± 0.01	0.02 ± 0.01	0.02	0.93	1.86
K	1	0.75 ± 0.02	0.118	0.04 ± 0.01	0.02 ± 0.01	0.02	0.82	2.27
Rb	1	0.69 ± 0.02	0.135	0.03 ± 0.01	0.01 ± 0.01	0.01	0.78	2.48
Cs	1	0.64 ± 0.02	0.148	0.03 ± 0.01	0.01 ± 0.01	0.01	0.79	2.65
Be	2	1.28 ± 0.02	0.053	0.08 ± 0.02	0.05 ± 0.02	0.06	1.57	1.12
Mg	2	0.96 ± 0.02	0.035	0.12 ± 0.02	0.18 ± 0.04	0.18	1.31	1.60
Ca	2	0.87 ± 0.02	0.052	0.15 ± 0.02	0.22 ± 0.05	0.22	1.00	1.97
Sr	2	0.82 ± 0.02	0.065	0.14 ± 0.02	0.19 ± 0.04	0.19	0.95	2.15
Ba	2	0.77 ± 0.02	0.080	0.12 ± 0.02	0.15 ± 0.04	0.16	0.89	2.22
Cu	11	1.28 ± 0.02	0.035	0.28 ± 0.03	0.42 ± 0.06	0.42	1.90	1.28
Ag	11	1.20 ± 0.02	0.045	0.25 ± 0.03	0.45 ± 0.06	0.45	1.93	1.44
Zn	12	1.40 ± 0.02	0.028	0.32 ± 0.03	0.48 ± 0.05	0.48	1.65	1.34
Cd	12	1.35 ± 0.02	0.032	0.35 ± 0.03	0.52 ± 0.05	0.52	1.69	1.51
Al	13	1.55 ± 0.02	0.022	0.45 ± 0.03	0.65 ± 0.05	0.65	1.61	1.43

Element	Group	r (Å)	ε (eV)	χ (calc)	χ (pred)	η (e/Å)	χ (Pauling)	r_cov (Å)
Ga	13	1.48 ± 0.02	0.028	0.38 ± 0.03	0.58 ± 0.05	0.58	1.81	1.36
In	13	1.42 ± 0.02	0.035	0.35 ± 0.03	0.55 ± 0.05	0.54	1.78	1.66
Si	14	1.52 ± 0.02	0.025	0.42 ± 0.03	0.62 ± 0.05	0.62	1.90	1.17
Ge	14	1.48 ± 0.02	0.028	0.40 ± 0.03	0.60 ± 0.05	0.60	2.01	1.22
Sn	14	1.42 ± 0.02	0.030	0.38 ± 0.03	0.68 ± 0.05	0.68	1.96	1.40
Pb	14	1.45 ± 0.02	0.025	0.40 ± 0.03	0.72 ± 0.05	0.72	2.33	1.46
P	15	1.58 ± 0.02	0.018	0.38 ± 0.03	0.55 ± 0.05	0.70	2.19	1.10
As	15	1.52 ± 0.02	0.022	0.42 ± 0.03	0.62 ± 0.05	0.64	2.18	1.19
Sb	15	1.48 ± 0.02	0.025	0.44 ± 0.03	0.65 ± 0.05	0.60	2.05	1.40
Bi	15	1.38 ± 0.02	0.035	0.42 ± 0.03	0.70 ± 0.05	0.50	2.02	1.46

Table S2 | DFT Convergence Benchmarks

System	Atoms	Cutoff (eV)	k-points	Energy (eV)	Force (eV/Å)	Time (hours)	Memory (GB)
1/1 Approximant	168	500	$4 \times 4 \times 4$	10^{-6}	0.01	0.5	4
2/1 Approximant	1,350	500	$2 \times 2 \times 2$	10^{-6}	0.01	24	64
3/1 Approximant	10,400	500	Γ-only	10^{-6}	0.01	48	256
Na Monolayer (1/1)	168 + 120	500	$4 \times 4 \times 1$	10^{-6}	0.01	1	8
K Monolayer (1/1)	168 + 120	500	$4 \times 4 \times 1$	10^{-6}	0.01	1	8
Pb Monolayer (1/1)	168 + 120	500	$4 \times 4 \times 1$	10^{-6}	0.01	2	8

System	Atoms	Cutoff (eV)	k-points	Energy (eV)	Force (eV/Å)	Time (hours)	Memory (GB)
Al Monolayer (1/1)	168 + 120	500	$4 \times 4 \times 1$	10^{-6}	0.01	2	8
Alloy ($Na_{0.9}Pb_{0.1}$)	168 + 120	500	$4 \times 4 \times 1$	10^{-6}	0.01	2	8

Table S3 | Kernel Polynomial Method Parameters

Parameter	Value	Description
System size N	168 – 10,400 atoms	Number of atoms in the system
Chebyshev moments M	2,000	Number of moments in Chebyshev expansion
Random vectors N_v	10	Number of random vectors for stochastic trace
Energy points	2,000	Number of energy points in DOS calculation
Energy resolution ΔE	0.02 eV	Spectral resolution ($2W/M$)
Bandwidth W	10 eV	Total energy range of the Hamiltonian
Jackson kernel	Yes	Damping kernel for Gibbs oscillation suppression

Parameter	Value	Description
Memory (10,400 atoms)	8 GB	Memory usage for sparse Hamiltonian
Time (10,400 atoms)	2 hours	Wall-clock time on 32 cores
Scaling	$\mathcal{O}(N)$	Linear scaling with system size

Table S4 | Bader Charge Analysis: Complete Results

Element	Initial Valence	Retained Charge	Charge Transfer	Hybridization Strength
Li	1.00	0.97 ± 0.02	0.03 ± 0.02	Very weak
Na	1.00	0.95 ± 0.02	0.05 ± 0.02	Very weak
K	1.00	0.93 ± 0.02	0.07 ± 0.02	Very weak
Rb	1.00	0.91 ± 0.02	0.09 ± 0.02	Very weak
Cs	1.00	0.90 ± 0.02	0.10 ± 0.02	Very weak
Be	2.00	1.85 ± 0.03	0.15 ± 0.03	Weak
Mg	2.00	1.82 ± 0.03	0.18 ± 0.03	Weak

Element	Initial Valence	Retained Charge	Charge Transfer	Hybridization Strength
Ca	2.00	1.78 ± 0.03	0.22 ± 0.03	Weak
Sr	2.00	1.75 ± 0.03	0.25 ± 0.03	Weak
Ba	2.00	1.72 ± 0.03	0.28 ± 0.03	Weak
Cu	11.00	10.2 ± 0.1	0.8 ± 0.1	Moderate
Ag	11.00	10.1 ± 0.1	0.9 ± 0.1	Moderate
Zn	12.00	11.2 ± 0.1	0.8 ± 0.1	Moderate
Cd	12.00	11.1 ± 0.1	0.9 ± 0.1	Moderate
Al	3.00	2.4 ± 0.1	0.6 ± 0.1	Strong
Ga	3.00	2.3 ± 0.1	0.7 ± 0.1	Strong
In	3.00	2.2 ± 0.1	0.8 ± 0.1	Strong
Si	4.00	3.1 ± 0.1	0.9 ± 0.1	Strong
Ge	4.00	3.0 ± 0.1	1.0 ± 0.1	Strong
Sn	4.00	2.9 ± 0.1	1.1 ± 0.1	Strong
Pb	4.00	2.8 ± 0.1	1.2 ± 0.1	Strong
P	5.00	3.8 ± 0.1	1.2 ± 0.1	Strong
As	5.00	3.7 ± 0.1	1.3 ± 0.1	Strong

Element	Initial Valence	Retained Charge	Charge Transfer	Hybridization Strength
Sb	5.00	3.6 ± 0.1	1.4 ± 0.1	Strong
Bi	5.00	3.5 ± 0.1	1.5 ± 0.1	Strong

Supplementary Notes

S1 | Computational Details

All DFT calculations were performed using VASP 6.3.2 with the projector augmented wave (PAW) method and the Perdew-Burke-Ernzerhof (PBE) generalized gradient approximation exchange-correlation functional. The plane-wave cutoff was set to 500 eV after convergence testing (Fig. S2a). Brillouin zone sampling employed Γ-centered Monkhorst-Pack grids with density 0.02 Å $^{-1}$ (Fig. S2b). Electronic convergence was accelerated using the block Davidson algorithm with a convergence threshold of 10^{-6} eV for total energy. Atomic positions were relaxed until forces were below 0.01 eV/Å (Fig. S2c). For surface calculations, a dipole correction was applied to cancel artificial electric fields across the slab.

S2 | Approximant Generation

The 1/1 and 2/1 cubic approximants were generated using the projection method from the six-dimensional icosahedral lattice. The 1/1 approximant ($a = 12.8$ Å) contains 168 atoms per unit cell with composition Al $_{100}$Pd $_{40}$Mn $_{28}$. The 2/1 approximant ($a = 20.7$ Å) contains approximately 1,350 atoms per unit cell with composition Al $_{850}$Pd $_{350}$Mn $_{150}$. The 3/1 approximant ($a = 33.5$ Å) contains approximately 10,400 atoms per unit cell and was used only for convergence testing.

S3 | Kernel Polynomial Method Implementation

The KPM implementation in the KITE library expands the spectral function in Chebyshev polynomials:

$$\rho(E) = \frac{1}{\pi\sqrt{1-\tilde{E}^2}} \sum_{m=0}^{M-1} \mu_m \, T_m(\tilde{E}) g_m$$

where $\tilde{E}$ is the rescaled energy in $[-1,1]$, T_m are Chebyshev polynomials, μ_m are Chebyshev moments computed via sparse matrix-vector multiplication, and g_m is the Jackson kernel

damping factor. The method achieves linear scaling $\mathcal{O}(N)$ with system size (Fig. S12c) and requires $\mathcal{O}(N)$ memory (Fig. S12d). Convergence is controlled by the number of Chebyshev moments M (Fig. S12a) and the number of random vectors N_v (Fig. S12b).

S4 | Machine Learning Model Architecture

The neural network for predicting pseudogap depth consists of:

- Input layer: 5 features (electronegativity, atomic radius, electron density, d-orbital occupancy, ionization potential)
- Graph convolutional layer: 64 hidden units with ReLU activation
- Attention layer: 32 units with softmax attention mechanism
- Two fully connected layers: 32 and 16 units with ReLU activation and dropout (0.2)
- Output layer: single unit with linear activation

The model was trained on 80% of the 25-element dataset (20 elements) and tested on the remaining 20% (5 elements). Training used the Adam optimizer with learning rate 0.001, mean squared error loss, and 500 epochs. The final model achieved $R^2 = 0.96$ on the test set and mean absolute error 0.018.

S5 | Error Analysis

All reported uncertainties are standard deviations from multiple calculations:

- DFT calculations: 5 independent calculations with different initial configurations
- KPM calculations: 10 independent random vector sets
- Structural parameters: 3 independent approximant structures
- Statistical distributions: 100 independent DFT calculations

Error bars in figures represent one standard deviation. For parameters without explicit error bars, uncertainties are estimated to be ±5% based on convergence tests.

Supplementary References

[1] G. Kresse, J. Furthmüller, *Phys. Rev. B* **54**, 11169 (1996).

[2] P. E. Blöchl, *Phys. Rev. B* **50**, 17953 (1994).

[3] J. P. Perdew, K. Burke, M. Ernzerhof, *Phys. Rev. Lett.* **77**, 3865 (1996).

[4] A. Weiße, G. Wellein, A. Alvermann, H. Fehske, *Rev. Mod. Phys.* **78**, 275 (2006).

[5] N. Marzari, D. Vanderbilt, *Phys. Rev. B* **56**, 12847 (1997).

[6] Z. Papadopolos, G. Kasner, J. Hafner, *Phys. Rev. B* **66**, 184207 (2002).

Supplementary Files

This is a list of supplementary files associated with this preprint. Click to download.

- Supplementarypaper.pdf